SLAC–PUB–5813
August 1993
(E)

MEASUREMENT OF THE A–DEPENDENCE OF DEEP–INELASTIC ELECTRON SCATTERING*

J. GOMEZ*, R. G. ARNOLD, P. E. BOSTED, C. C. CHANG♯
A. T. KATRAMATOU, G. G. PETRATOS°, A. A. RAHBAR,
S. E. ROCK, A. F. SILL◇, AND Z. M. SZALATA
Department of Physics, The American University, Washington D.C. 20016

A. BODEK, N. GIOKARIS▷
– University of Rochester, Rochester N. Y. 14627

D. J. SHERDEN
Stanford Linear Accelerator Center
Stanford University, Stanford, CA 94309

B. A. MECKING*
Universität Bonn, D–5300 Bonn, West Germany

and

R. M. LOMBARD–NELSEN
CE–Saclay, DAPNIA/SPhN, 91191 Gif/Yvette, France

Submitted to *Physical Review D*

---

*Work supported in part by Department of Energy contract DE–AC03–76SF00515.
Present addresses: *CEBAF, Newport News, VA 23606.
°SLAC, Stanford University, Stanford, CA 94309.
◇Department of Physics, Texas Tech, Lubbock, TX 79409.
▷FERMILAB, Batavia, IL 60510.
Permanent address: ♯Dept. of Phys., U. of Maryland, College Park, MD 20742.

ABSTRACT

Cross sections for deep inelastic electron scattering from liquid deuterium, gaseous ^{4}He, and solid Be, C, Al, Ca, Fe, Ag, and Au targets were measured at the Stanford Linear Accelerator Center using electrons with energies ranging from 8 to 24.5 GeV. These data cover a range in the Bjorken variable x from 0.089 to 0.8, and in momentum transfer Q^2 from 2 to 15 (GeV/c)^2. The ratios of cross sections per nucleon $(\sigma^A/\sigma^d)_{is}$ for isoscaler nuclei have been extracted from the data. These ratios are greater than unity in the range $0.1 < x < 0.3$; while for $0.3 < x < 0.8$, they are less than unity and decrease logarithmically with atomic weight A, or linearly with average nuclear density. No Q^2 dependence in the ratios was observed over the kinematic range of the data. These results are compared to various theoretical predictions.

I. INTRODUCTION

The structure functions for charged lepton scattering from a nucleon are related to the cross section by

$$\frac{d^2\sigma}{d\Omega dE'} = \frac{4\alpha^2 (E')^2}{Q^4} \cos^2\left(\frac{\theta}{2}\right) \left[\frac{F_2(x,Q^2)}{\nu} + \frac{2F_1(x,Q^2)}{M} \tan^2\left(\frac{\theta}{2}\right)\right] , \quad (1)$$

where $\alpha = e^2/4\pi \sim 1/137$ is the fine structure constant, the four momentum transfer squared is $Q^2 \equiv -q^2 = 4EE' \sin^2(\theta/2)$, the initial and scattered lepton energies are E and E', the energy of the virtual photon is $\nu = E - E'$, the Bjorken scaling variable is $x = Q^2/(2M\nu)$, M is the nucleon rest mass, θ is the detected lepton scattering angle, and F_1 and F_2 are the deep inelastic structure functions. The polarization of the virtual photon $\epsilon = \left[1 + 2\left(1 + [\nu^2/Q^2]\right) \tan^2(\theta/2)\right]^{-1}$ is often used along with x and Q^2 to completely specify the kinematics. Significant differences in the cross sections of heavier nuclei compared to deuterium have been observed in muon [1–6] and electron [7–9] scattering. This was somewhat unexpected both in the quark-parton model and in QCD, since the energy scale for binding nucleons in nuclei is much lower than the energy scale for the virtual photon-quark interaction. It was believed that in the kinematic region of $0.1 \leq x \leq 0.6$, the inelastic structure function per nucleon F_2^A of a nucleus of atomic weight A was simply related to the inelastic structure functions F_2^p and F_2^n of a free proton and neutron by

$$A \cdot F_2^A = Z \cdot F_2^p + (A - Z) \cdot F_2^n . \quad (2)$$

At small x or Q^2, shadowing [10–12] was expected to decrease the structure functions of nuclei, due to either the virtual photon having a hadronic component or overlapping of nucleons due to relativistic contraction. For x larger than about 0.6, the motion of nucleons within the nucleus (Fermi smearing), convoluted with the sharply decreasing value of F_2^p and F_2^n with increasing x, will effectively increase the nuclear structure function relative to that of the nucleon structure function[13].

Early inelastic lepton scattering experiments using nuclear targets searched for shadowing [14–15] in the region of $x \leq 0.2$ and $Q^2 \leq 1.6$ (GeV/c)^2, where the quark-parton model is not expected to hold and where shadowing was expected to be important. Shadowing in electroproduction at $Q^2 \sim 1$ (GeV/c)^2 was found to be significantly smaller than in photoproduction. Since shadowing was expected to rapidly disappear with increasing Q^2, further investigations on the A-dependence of the structure functions for larger values of x and Q^2 were not undertaken, and Eq. (2) was assumed to hold. Later, high Q^2 muon and neutrino scattering experiments were designed to use nuclear targets because such targets were easier to construct than hydrogen or deuterium targets with the required number of scattering centers. However, it was implicitly assumed that, aside from Fermi motion corrections, such experiments measured the structure functions of free nucleons.

In 1983, the European Muon Collaboration (EMC) reported [1] their measurements of the ratio of the cross sections per nucleon of iron to that from deuterium. The ratios were clearly different from unity, being greater than unity at low x and dropping below unity for x greater than about 0.3. The rise beyond $x = 0.6$ can be accounted for in terms of Fermi motion. Re-analysis of old SLAC data from target end caps confirmed [7–8] this finding for $x \geq 0.15$. This A-dependence of the structure functions became known as the EMC effect. If the nucleon inelastic structure functions are to be extracted from lepton scattering data off nuclear targets, such as iron, they must be corrected for the EMC effect.

The experiment reported in this article, designated as SLAC–E139, was designed to examine the dependence of the EMC effect on the kinematic variables x and Q^2, as well as on the atomic number of the target nucleus. Preliminary results on the ratio of cross sections have been reported earlier [9]. Here we present

the final results on cross sections and cross-section ratios using an improved radiative correction procedure. The remainder of this paper describes the apparatus (Sec. II), the data analysis (Sec. III), and the experimental results and their comparison to some representative theoretical models (Sec. IV).

II. EXPERIMENTAL APPARATUS

A schematic view of the experimental setup is shown in Fig. 1 . The incident electron beam produced by the Stanford Linear Accelerator [16], was focused onto a target assembly located in SLAC End Station A. Targets of liquid deuterium, gaseous ^{4}He, and solid Be, C, Al, Ca, Fe, Ag, and Au were used. Scattered electrons were detected in the SLAC 8-GeV/c magnetic spectrometer. It was instrumented with ten planes of multiwire proportional chambers to allow event reconstruction. Electron separation from background (predominantly π-mesons) was accomplished with a nitrogen-filled threshold Čerenkov counter and a 20-radiation-length (r.l.) thick segmented lead-glass electromagnetic calorimeter.

Signals from the various detectors were sent to Counting House A to be processed through fast electronic logic. A Digital Equipment Corporation (DEC) VAX 11/780 computer logged onto magnetic tape both specific information about each event and general information about the experiment—such as scalars, magnet status, and amount of incident electron beam received. The same computer also provided partial analysis of the data during the course of the experiment.

A. Electron beam transport and monitoring

Electrons were accelerated to energies ranging between 8.0 and 24.5 GeV at up to 180 pulses per second by the Stanford Linear Accelerator. The beam pulses were nominally 1.6 μsec long for energies ranging from 8 to about 21 GeV. For the

24.5 GeV incident energy, the beam pulses were about 160 nsec long. The nominal centroid of the beam energy is known [17] to an accuracy of $\pm 0.1\%$. This uncertainty is correlated with the uncertainty in central spectrometer momentum discussed in Sec. II.D. The beam energy uncertainty contributed an error of up to $\pm 0.5\%$ to the absolute cross section, but cancelled in the ratio of cross sections with different targets.

The energy spread was typically limited to $\pm 0.25\%$ by high power slits. A SLAC elastic e-p scattering experiment [18] using the same accelerator and beam line before and after this experiment has reported that their measured elastic peak width was compatible with a beam energy spread smaller than the maximum allowed by their slit settings of about $\pm$ 0.2%. Consequently, we have assigned an uncertainty in the beam energy of $\Delta E/E = \pm 0.1\%$ due to fluctuations within the opening of the slits. The resulting uncertainty in the measured cross sections varied from less that $\pm$ 0.1% to $\pm$ 0.5%. The uncertainty in the cross section ratios caused by this source of error mostly cancels due to the rapid changing of targets, and is estimated to be less than 0.3%.

Beam position and angle at the target were checked and adjusted if necessary by two independent systems. The first consisted of two zinc-sulfide fluorescent screens (RS1-RS2 in Fig. 1), which were inserted in the beam every few hours. With a separation of 10 meters and a resolution of ± 1 mm, the angular resolution was ± 0.2 mr. The resulting uncertainty in the absolute cross sections varied with kinematics from $\pm$ 0.3% to $\pm$ 1.5% (at the largest value of x). The maximum uncertainty in the cross section ratios varied with kinematics from $\pm 0.1\%$ to $\pm 1\%$.

The second system measured the beam position and profile in both the vertical and horizontal directions continuously during the experiment. It was composed of two planes of secondary emission wire arrays located 2 meters before the target (see Fig. 1). Each plane consisted of a series of 0.13-mm diameter aluminum wires

spaced at 0.4 mm intervals, whose beam-induced secondary emission signals were recorded each beam pulse. With this information, a dedicated LSI–11 computer continuously steered the beam onto the target center within ±1 mm.

The beam flux was measured with two independent toroidal charge monitors [19]. Each monitor consisted of: (a) one toroidal pulse transformer and associated pre-amplifier; (b) two independent sets of the electronics necessary to amplify, digitize, and accumulate the signals; and (c) a calibration unit. The waveform produced in the damped resonant circuit connected to the toroid was amplified and then measured by two independent units: the old system [19] recorded the signal near its peak while the newer system recorded the integrated value of one cycle. Error analysis [19,20] of the old system shows accurate measurements for all the beam pulse lengths of this experiment. The new system was read out every beam pulse by the same LSI–11 computer used for beam steering. Fluctuations in the charge monitors were checked by comparing the readings from all the units and found to agree at the ± 0.2% level. We have assigned a ± 0.2% relative uncertainty in the cross sections due to this source of error. This error mostly cancels in the ratios of cross sections.

Each toroid was equipped with a calibration unit which simulated the electron beam by sending a precisely known charge through a single additional turn of wire passing through the toroid. The calibration and zero drift of the two toroids were systematically checked during the experiment. The absolute accuracy of the charge monitor's calibration units were not checked during this experiment. Previous measurements [21,22], which compared the readings of the charge monitors to those from a Faraday cup, have reported an absolute uncertainty of ± 0.5% in the charge measurement. We have assigned an overall uncertainty of ± 0.5% to the cross sections due to this source of error. This error cancels in the ratio of cross sections.

B. Targets

Targets of liquid deuterium, gaseous ^{4}He, and solid Be, C, Al, Ca, Fe, Ag, and Au of various thicknesses were used. The target assembly (shown in Fig. 2) rotated about its vertical axis and moved up and down under remote computer control to quickly bring a specific target into the path of the beam. During the experiment, targets were changed every few minutes to minimize systematic errors in the ratios of cross sections.

The major components of the deuterium and helium targets are shown in Fig. 3. The deuterium and helium were pumped rapidly through the target cells to minimize any change in their densities due to beam heating. In both cells, the fluid flowed through a liquid hydrogen heat exchanger at 21°K, and then into the target cell's inner mylar tube, returned through the annulus defined by the inner cylinder and the cell wall, and then back to the heat exchanger. The deuterium was in a liquid state under a pressure of 2 atm to minimize local boiling due to heat deposited by the beam. The helium was in a gaseous state under a pressure of 25 atm. To calculate the target density, the average temperature of the deuterium and helium targets—as well as their pressure—were measured by vapor pressure bulbs, platinum resistors, and pressure transducers to an accuracy of $\pm 0.6\%$. The calibration coefficients [23] used to determine the deuterium density from the measured pressure and temperatures are accurate to $\pm$ 0.6%. In the case of helium, these coefficients [24] are accurate to $\pm$ 2%. The uncertainty in the deuterium and helium target lengths is $\pm$ 0.4%. We have assigned systematic uncertainties to the cross sections of $\pm$ 2.1% in the case of helium and $\pm$ 0.9% in the case of deuterium. These errors contribute to both the cross sections and the cross-section ratios.

Data obtained with the empty deuterium and helium cells in the beam were used to determine the contributions from the end caps of the full cells to the

measured cross sections. The composition and dimensions of the full and empty deuterium and helium cells are given in Table 1.

Local density changes due to beam heating in the deuterium and helium targets were carefully monitored. Data from these targets were taken with at least two different beam repetition rates at each kinematic setting. The beam profile was constantly monitored and recorded to avoid a tightly focussed beam at the targets. Additionally, high statistics studies of beam-induced density changes in these targets were done. Based on the comparison of the corrections predicted by various methods, we have assigned a relative uncertainty to the cross sections of $\pm$ 1.4% in the case of helium and $\pm$ 0.5% in the case of deuterium. Details of this procedure are given in Sec. III.C.1.

The solid targets available in the experiment and their thickness are given in Table 2. The uncertainty in the target thicknesses ranged from $\pm$ 0.5% (Be) to $\pm$ 2.3% (Au). The solid targets were cooled by conduction through the target assembly that was in contact with the liquid hydrogen reservoir at 21 °K. Density changes from target heating were found to be negligible.

C. Spectrometer and particle detectors

Particles scattered from the target were analysed using the SLAC 8 GeV/c magnetic focusing spectrometer [25,26] shown schematically in Fig. 4. The central angle of the spectrometer was known to within $\pm$0.10 mr. The central momentum of the spectrometer was known to $\pm$0.05% from Floating Wire measurements [27] and also from elastic peak studies [18].

The particle detection system is shown schematically in Fig. 5. Its purpose was to: (a) provide event triggers for all electrons scattered into the spectrometer acceptance, (b) discriminate electrons from background consisting predominantly of π-mesons, and (c) allow kinematic reconstruction of an event. Particles scattered

into the spectrometer, after passing through Q83, traversed a threshold Čerenkov counter filled with nitrogen at subatmospheric pressure. Next they passed through ten planes of multiwire proportional chambers which provided information about the trajectories of the scattered particles and hence allowed their kinematic reconstruction. Finally, the scattered particles entered a 20-r.l. thick electromagnetic calorimeter whose main purpose was to differentiate electrons from background.

1. Čerenkov counter

The threshold Čerenkov counter was 2.79-meters long with 0.04-cm thick aluminum windows at each end. It was placed forward of all other detectors to minimize the amount of material before the counter, and hence reduce the probability that knock-on electrons produced by π-mesons would fire the counter.

Čerenkov light produced by a charged particle with momentum above threshold was focused by a four-segment front-face mirror directly onto a 5-inch diameter Amperex XP2041 photomultiplier. The photomultiplier front face was coated with a wavelength shifter [28] to increase the photomultiplier detection efficiency in the ultraviolet.

The counter contained nitrogen gas at an average pressure of 590 mm Hg, which corresponds to momentum thresholds of about 0.024 and 6.5 GeV/c for electrons and pions respectively. This operating pressure resulted in an efficiency for electrons of 99.5%, with an efficiency of less than 0.01% for pions with momentum less than 6.5 GeV/c.

2. Multiwire proportional chambers

A set of ten planes of multiwire proportional chambers [29] was used to reconstruct the trajectories of the scattered particles in the region of the spectrometer focal planes. These chambers replaced the hodoscope system [21] used with the

8 GeV/c spectrometer by previous experiments. They increased the maximum detectable momentum bite of the spectrometer to about ± 4% from the previous value of ± 2%. With ten chambers, the track reconstruction efficiency was found to be 99.8% with negligible background of false tracks due to spurious hits. Five "P" chambers with horizontal wires measured momentum and azimuthal angle. Five "T" chambers with wires alternately ±30° to the vertical were used to measure the horizontal scattering angle. The anode wires were connected to amplifiers, followed by two one-shot delays, each timed to about 450 nsec. The first one-shot delay determines the dead time of each wire. When the main experimental trigger fired, a common gate (100-nsec wide) latched the delayed signals for subsequent readout by CAMAC.

3. Lead-glass electromagnetic calorimeter

A lead-glass electromagnetic calorimeter [30] was used to separate electrons from background (predominantly π-mesons). This counter, made of F2 lead glass, was segmented longitudinally in two sections:

(1) a preradiator (PR) consisting of six blocks that are 10.4-cm thick (3.23 r.l.), 15.8-cm wide, and 32-cm tall, each with a 5-inch diameter Amperex XP2041 tube, followed by

(2) a total absorber (TA) composed of four blocks that are 54-cm thick (16.77 r.l.), 25-cm wide, and 36-cm tall, each viewed by a 9-inch diameter Amperex 60DVP tube (see Fig. 5).

The PR and TA were treated as two separate counters for the purpose of generating an event trigger. The counter was built for a previous experiment [31]; it was refurbished to improve the counter resolution from about $\sigma = 12\%/\sqrt{E}$ to $8\%/\sqrt{E}$. The discriminator thresholds on the signals for both counters were set high enough to reject most pions, but low enough to be very efficient for electrons. The TA,

because of its long length and its position at shower maximum, had a measured efficiency for electrons of 99.9%. The PR, because of its short length and its position at the beginning of the shower, had a measured efficiency of 98.5%.

4. Electronics and data acquisition system

The electron trigger was designed to be close to 100% efficient for electron events, while being as insensitive as possible to background. It was formed by a coincidence between the TA and either the PR or the Čerenkov (CK) counters. The TA combined high efficiency for electrons and low efficiency for other particles. The combined PR and CK also had extremely high electron efficiency.

Analog signals from the Čerenkov counter and the electromagnetic calorimeter were split by linear fan-out units: (1) to measure the energy, using a charge-integrating analogue-to-digital converter (ADC); (2) to measure time and number, using a dead-timeless discriminator whoes outputs went to a time-to-digital converter (TDC), a latch, and a scaler; and (3) to construct the trigger using linear sums $\sum$PR and $\sum$TA that went to discriminators. The $\sum$PR selected particles that had deposited greater than minimum ionization. The $\sum$TA discriminator selected particles that had made large electromagnetic showers. The discriminated $\sum$PR and CK signals were ORed together, and went to the electron trigger coincidence. A low rate "random" trigger was used to monitor backgrounds and measure pedestals.

All discriminators were of the "burst guard" type to minimize dead time and were set for an output pulse 15-nsec wide. The width of the electron coincidence was set to 20 nsec. Additional electron coincidences with output widths of 40 and 60 nsec were scaled and used to estimate electronic trigger dead time. A straight line parametrization of the scaler values of these three coincidences was done to find the number of events that would have been obtained if the event coincidence

had an output pulse width of zero nanoseconds (no dead time). Corrections of up to 0.8% were applied, with more typical corrections being on the order of 0.1% to 0.3%. These corrections were consistent with the number of two-electron track events in the wire chambers, as discussed below.

The data acquisition system could handle, at most, one event per beam pulse. Additional events were counted, but not recorded. The over one-event-per-beam-pulse corrections to the experimental data were evaluated by taking the ratio of total events recorded in scalers to the number of events recorded on tape. The over one-event-per-beam-pulse correction factor ranged in value from 1.0 to about 1.30. On average, the value of this correction was less than about 1.12, with essentially no error.

The data acquisition system [32] consisted of a dedicated DEC PDP–11/04 computer connected as the terminator for the UNIBUS of a VAX 11/780. The PDP read the event data and wrote it to shared memory space in the VAX, and then the VAX logged the data on magnetic tape. The VAX also read, controlled, and recorded the status of the target, magnets, high voltages and beam. It analysed a sample of the events online, and calculated cross sections and ratios of cross sections, which were used to guide the course of the experiment.

III. DATA ANALYSIS

The principal steps in the analysis to convert the raw data logged on magnetic tape into differential inelastic cross sections and cross sections ratios were:

A. Event identification;

B. Calculation of spectrometer acceptance function;

C. Determination of calculated and measured corrections; and

D. Calculation of cross sections and cross section ratios.

The first three points above are discussed below while discussion of cross sections and cross section ratios is presented in Sec. IV.

A. Event identification

Event identification is comprised of: (1) electron identification and separation from the predominantly pion background, using the segmented lead-glass electromagnetic calorimeter and the threshold Čerenkov counter; (2) reconstruction of particle tracks from wire chamber data; and (3) reconstruction of the event kinematics at the target with a model of the 8 GeV/c spectrometer.

1. Event identification by energy deposition

Electrons will produce an electromagnetic cascade and deposit all their energy within the electromagnetic calorimeter. The vast majority of hadrons and all muons will either leave minimum ionizing energy (~ 0.4 GeV) or hadronic shower near the end of the counter, and deposit only a small portion of their energy. We calculated the ratios R^{SH} of the energy deposited by the detected particle in the shower counter (SH) to the particle momentum P, reconstructed from the magnetic spectrometer information. Thus $R^{SH} \sim 1$ for an electron and $\ll 1$ for most other particles. The energy deposited by a given track in the electromagnetic calorimeter was calculated using only those PR and TA blocks located within 1 r.l. of the track. To avoid loss of resolution due to shower leakage, particles hitting the counter within 1.35 r.l. from the counter's periphery were discarded. This cut limited the solid angle of the spectrometer.

The lead glass was calibrated using the measured electron energy from the spectrometer. To account for the position dependence of the light collection, each PR block was partitioned into eight segments (two vertical columns by four rows), while each TA block was partitioned into twelve segments (three vertical columns by four rows). Calibration coefficients related the pulse heights measured in the ADCs to the energies deposited in a particular segment. They were determined by optimizing the electron energy resolution using a linear least-square fitting

technique. The calibration coefficients were found to be independent of central spectrometer momentum P_0, as expected.

Figure 6 shows logarithmic plots of R^{SH} for a π/e ratio ~ 80 and $E' = 3.125$ (worst case). The total spectra is shown in (a) while (b) requires no Čerenkov signal (pions) and (c) requires a Čerenkov signal (electrons). In Fig. 6(c), the electron signal at $R^{SH} = 1$ is more than two orders of magnitude larger than the background. The minimum ionizing peak from muons and noninteracting hadrons that should appear at ~ 0.1 is cut off at ≈ 0.2 by the trigger discriminator threshold. The background subtraction is described in Sec. III.A.3.

An electron candidate had to have $R^{SH} \geq 0.74$. The cut was chosen to have at least 99.9% efficiency for electrons, while excluding as many pions as possible, as shown in Fig. 6. The cut was kept fixed, since even though the electron peak becomes narrower at higher scattered electron energy, the π/e ratio is smaller, and additional pion rejection is not needed. No individual cuts in the energy deposited by an event in the PR or TA sections of the counter were found necessary to separate electrons from background.

2. Čerenkov counter efficiency

Figure 7 shows several Čerenkov ADC spectra obtained from the deuterium target. Figure 7(a) corresponds to data taken at the worst case kinematics ($\pi/e \sim 80$). Figure 7(b) corresponds to data taken at $E' = 7.878$ GeV that is above pion momentum threshold (6.5 GeV/c) in the Čerenkov counter. Two histograms are shown for each kinematic point. Events shown in histograms labeled 1 (dotted line) were required to have a single track within the spectrometer acceptance. Events shown in histograms labeled 2 (solid line) were required to meet the additional criterion of $R^{SH} \geq 0.74$.

In Fig. 7(a), the large pedestal signal corresponds to pions with momenta below the threshold of the Čerenkov counter. Events to the left of the vertical arrows are below the Čerenkov discriminator threshold, and come only from the PR–TA coincidence in the trigger. The small peak located around channels 30 to 35 originates when the Čerenkov counter starts contributing to the trigger in a high π/e environment. An incoming pion has a probability of $\sim 1\%$ of triggering the Čerenkov counter through the production of low-energy knock-on electrons or scintillation in the gas. Events of this type will be characterized by a relatively small signal in both Čerenkov and Shower Counters. The removal of these events by the $R^{SH} \geq 0.74$ cut is the reason for the observed reduction at the low side of the Čerenkov ADC spectrum when comparing histograms 1 and 2 in Fig. 7(a). The difference between histograms 1 and 2 in Fig. 7(b) is due to the smaller amount of Čerenkov light produced by pions just above threshold. From the observed width of these spectra, we concluded that, on average, five photoelectrons were produced by an electron passing through the counter.

Electron events were required to have produced a signal in the Čerenkov counter above discriminator threshold (arrow in Fig. 7). The electron efficiency of this cut was measured with data from kinematic points with low π/e ratio, and requiring a single track in the chambers and a high cut on shower energy ($1.0 \leq R^{SH} \leq 1.3$). The Čerenkov measured efficiency for electrons was 99.5%, with no statistically significant variation with track position. This is consistant with the mean of five photoelectrons and the cut, including the one photo-electron signal.

3. Event misidentification

For those kinematic points with high π/e ratio or central spectrometer momentum above the Čerenkov momentum threshold for pions, there was some misidentification of background events as electrons. These pions fired the Čerenkov counter

through the production of knock-on electrons, scintillation of the nitrogen gas or because they had momentum above the pion threshold and also, in an uncorrelated manner, produced a large hadron shower in the shower counter. Figure 6(b) shows the normalized electromagnetic calorimeter spectrum R^{SH} for events which did not have a Čerenkov signal (pions), while Fig. 6(c) shows the same spectrum for events with a Čerenkov signal above threshold (mostly electrons) for the kinematic point with the highest π/e ratio. The shape of the R^{SH} pion spectrum is independent of the Čerenkov signal, and thus the properly normalized pion spectra from Fig. 6(b) can be subtracted from Fig. 6(c) to yield the pure electron spectrum. In order to determine the normalization, two regions were defined in each spectrum by the cuts shown in Fig. 6. The minimum normalized energy required for an electron event defined regions 2 and 4 ($R^{SH} \geq 0.74$). The background-dominated regions 1 and 3 were defined by a cut in R^{SH} at 0.3. This cut was chosen to be as low as possible and yet be free from effects due to trigger thresholds. The expected number of background events under the electron peak (N_4) was given by $N_4 = (N_3/N_1)\,N_2$, where N_i represents the number of events in the i^{th} region. The dashed line in Fig. 6(c) shows the shape of the normalized pion spectra when the Čerenkov signal was required. Corrections ranged from negligible (below 0.1%) to about 0.3% at the point with the highest π/e ratio.

4. Tracking

The basic task of the track-finding algorithm was to efficiently find the electron track associated with an event without finding spurious tracks. The detector environment often had large amounts of soft room background that generated single random hits. Also, under some conditions, there could be two or more real particle tracks, (either two electrons, or an electron and a pion) for a single event trigger. The tracking procedure has been described elsewhere [29]; hence, we only present a brief description here.

Because of the high efficiency of individual chambers ($\sim$ 95%), 99.4% of the electrons had hits on at least seven of the ten wire chambers. To minimize the time required to find a track, a search was done first for tracks with a minimum of three P-type, three T–type, and at least a total of seven chambers. If no tracks were found, the minimum requirements were lowered to two chambers of each type and a total of six chambers. Finally, if a third search was necessary, the total number of chambers required on a track were reduced from six to five. If the last search was unsuccessful, the event was classified as a no-track event. Tracks were first searched for in the vertical direction using the P-type chambers only. Next, this information was used to find the horizontal component of a track in the T–type chambers. Electron tracks were required to intersect the electromagnetic calorimeter at least 1.35 r.l. from its periphery and to deposit a large amount of energy near the intersection point.

In general, tracking performance depended on the ratio of background to electrons, true event rate, and beam tuning (which affects the random single rates).

Examples of the performance of individual wire chambers and of the tracking are presented in Tables 3 and 4. Data from two separate kinematic points are shown for the deuterium target. Data set 1 is from the kinematic point with $x = 0.4$, $Q^2 = 5.0$ (GeV/c)^2, and $\epsilon = 0.723$. This run was characterized by a noisy environment. The over one-event-per-beam-pulse correction was about 1.30, one of the highest in the experiment. Data set 2 is from the kinematic point with $x = 0.089$, $Q^2 = 2.0$ (GeV/c)^2, and $\epsilon = 0.391$. This point is characterized by a π/e ratio of about 80, the largest in the experiment. In Table 3 we observe that the individual wire chamber inefficiencies never exceeded 10%. The average chamber inefficiency over all chambers was less than 5%. Table 4 shows that the tracking inefficiency (as indicated by the percentage of total number of electron events with no-tracks) starts increasing when tracks are required to have more than about

seven chambers. At least 99.4% of all tracks had seven or more chambers with hits, with typically $\sim 0.1\%$ 5–chamber and 6–chamber tracks.

Most of the $< 0.5\%$ of the otherwise good electron events which failed to have a track were observed to be just scraping the upper edges of the chambers, and thus outside the acceptance. The remaining inefficiency of $\leq 0.2\%$ was apparently related to a minor hardware problem with the chamber readout module.

High counting rates could cause multiple particles (tracks) in an event. As seen in Table 4, two-track events were less than 6% of total number of events and three-track events were less than 0.3%. Most multitrack events consisted of an electron and a pion. If the tracks pointed to distinct blocks of the shower counter, complete identification of all tracks as pions or electrons was possible. If two or more tracks pointed to the same block, or close together in adjacent blocks, the total normalized energy in the shower counter was used to determine the number of electron and pion tracks. Individual track identification was not possible, and a statistical procedure was used to include these events. The number of multi-electron events from the tracking agreed with the values expected from the trigger electronics dead time (see Sec II.C.4) to better than 0.1%.

5. *Event kinematics reconstruction*

Kinematic quantities at the target were reconstructed for each detected event using the optical properties of the 8 GeV/c spectrometer. For each of those events determined to be an electron, reconstructed kinematic quantities were individually stored so that we could:

(*a*) obtain the 8 GeV/c spectrometer acceptance function, and

(*b*) divide the spectrometer momentum-angle bite for each kinematic point into various regions and evaluate cross section ratios for each of those regions.

An optical model of the 8 GeV/c spectrometer, derived from measurements performed circa 1967 with a 6 GeV SLAC electron beam [25,33] was used to transform tracks measured in the chambers into kinematic quantities at the target, measured with respect to the spectrometer central ray: the horizontal angle θ_s, the vertical angle ϕ_s, and δ_s, the fractional deviation of the momentum from the central value P_0. These quantities are related to the production azimuthal angle (θ), the polar angle (ϕ), and the momentum P by $\tan\phi = \tan\phi_s / \sin(\theta_0 + \theta_s)$, $\cos\theta = \cos(\theta_0 + \theta_s)\ \cos\phi_s$, and $P = P_0(1 + \delta_s)$, where θ_0 is the spectrometer central azimuthal angle. We found [34] it necessary to correct the δ_s and θ_s values obtained from the 6 GeV/c reconstruction matrix by

$$\delta_s = \delta_s^6(1 + 0.0071\ \delta_s^6)\ , \tag{3}$$

$$\theta_s = \theta_s^6(1 - 0.0006\ \theta_s^6)\ , \tag{4}$$

where δ_s^6 and θ_s^6 are the 6 GeV/c optical model momentum deviation and spectrometer horizontal angle respectively, and δ_s and θ_s represent the values that these quantities should actually have. This correction is equivalent to adjusting some of the second order terms of the transformation. These terms recently [27] have been more accurately measured by using a floating wire technique. The difference between the acceptance derived from the floating wire measurement and the previously used value [34] is within the errors of the measurement, and no correction has been applied.

B. Spectrometer acceptance

The spectrometer acceptance is determined by the various spectrometer apertures and by the detector geometry. The usable spectrometer solid angle is within the region $-4 \leq \delta_s\ (\%) \leq 3.5$, $-8 \leq \theta_s\ (\text{mr}) \leq 8$, and $-30 \leq \phi_s\ (\text{mr}) \leq 30$. The spectrometer acceptance is also a function of target length, being different for

extended targets (deuterium and helium) than for the thin solid targets. In the case of extended targets, the acceptance changes with spectrometer angle.

1. Thin-target acceptance

The thin-target spectrometer acceptance was determined directly from the experimental data and the optical properties of the spectrometer. A fiducial region of size $-1.5 \leq \delta_s$ (%) ≤ 1.5, $-3.0 \leq \theta_s$ (mr) ≤ 3.0, and $-15.0 \leq \phi_s$ (mr) ≤ 15.0 is free from the effect of any spectrometer aperture. The acceptance of this region depends only on the accuracy of our optical model. The acceptance outside the fiducial region was obtained by extrapolating the cross section in the fiducial region using renormalized models of the structure functions, corrected for preliminary values of the EMC effect. The systematic error in this procedure was negligible because: (1) the structure functions vary slowly with kinematics inside the small angular and momentum acceptance of the spectrometer, and (2) we averaged over many kinematic settings.

The electron events were accumulated in a 3-dimensional histogram in θ_s, ϕ_s, and δ_s. The notation $\Delta\Omega\Delta\delta \equiv \Delta\theta_s\Delta\phi_s\Delta\delta_s$ is used for the acceptance of a bin. The unnormalized fractional acceptance of the i^{th} bin was then given by

$$(\Delta\Omega\Delta\delta)_i^U = \frac{\sum_k N_{ik}^{\rm exp}}{\sum_k N_{ik}^{\rm model}} \tag{5}$$

where the summation over k includes all thin targets and kinematic points, and $N_{ik}^{\rm exp}$ is the number of events that fall in the i^{th} bin during the experiment and $N_{ik}^{\rm model}$ is the corresponding number of events predicted from the model.

This unnormalized acceptance was normalized to the fiducial region using

$$(\Delta\Omega\Delta\delta)_i = (\Delta\Omega\Delta\delta)_i^U \left[\frac{(\Delta\Omega\Delta\delta)_{\rm Fid}}{\sum_{\rm Fid\,j} (\Delta\Omega\Delta\delta)_j^U} \right] \tag{6}$$

where $(\Delta\Omega\Delta\delta)_i$ is the normalized acceptance of the i^{th} bin, $\sum_{\rm Fid\,j} (\Delta\Omega\Delta\delta)_j^U$ is the unnormalized acceptance of the fiducial region as calculated from Eq. (5) while $(\Delta\Omega\Delta\delta)_{\rm Fid}$ is the acceptance of the fiducial region as calculated from its chosen dimensions [$(\Delta\Omega\Delta\delta)_{\rm Fid} = 0.54$ msr $\cdot$ % in our case].

The inelastic model cross sections used in the calculation of the thin-target acceptance function were checked for each of the kinematic points. The measured value of the unrenormalized fractional acceptance in each of bins in the fiducial region [from Eq. (5) without the sum over kinematic points] was compared with its expected value. Agreement was within $\pm$ 2% with statistical errors of $\pm$ 1.5%. Averaged over all kinematics the agreement was 0.5%. This implies that the acceptance shape over the spectrometer momentum-angle bite is probably correct to $\pm$0.5%.

Two experimental thin-target acceptance functions had to be calculated from the data due to a change in the vacuum pipe in one of the magnets. The values of the total acceptance obtained in these two cases were 4.344 ± 0.020 and 4.542 ± 0.014 msr $\cdot$ % (statistical error only).

2. *Deuterium and helium targets acceptance*

The spectrometer acceptance for an extended target is a function of both the target length and spectrometer angle. It was not possible to obtain the acceptance of the deuterium and helium targets directly from the data, as in the case of the solid targets, since each of the kinematic points available in this experiment had a different spectrometer angle, and no kinematic point by itself had data with

enough statistical precision. A Monte Carlo model of the 8 GeV/c spectrometer was used to obtain the ratios of the deuterium and helium targets acceptance to the acceptance of a thin-target. It included all spectrometer apertures and represented each magnetic element by TRANSPORT [35] coefficients. Simulated electrons that passed all aperatures and hit the detector were reconstructed back to the target using the same method as in the data analysis.

Figure 8 shows the results of these simulations. The Monte Carlo predictions for the ratios of the long target acceptance to the thin-target acceptance were parametrized in terms of spectrometer angle θ_0 (in degrees) and target length L (in cm) as

$$\frac{(\Delta\Omega\Delta\delta)_{\rm Long}}{(\Delta\Omega\Delta\delta)_{\rm Thin}} = 1 - 1.5 \times 10^{-9}\ L^{3.5}\theta_0\ . \qquad (7)$$

All data in this experiment were taken between 11° and 23°. The maximum corrections applied to the thin-target acceptance were approximately 0.3% and 0.1% for helium and deuterium respectively.

C. Corrections to experimental data

1. *Deuterium and helium target densities*

The average heating of the entire deuterium and helium target by the beam was measured by the resistors and vapor pressure bulbs. However, because of the high instantaneous beam currents used in this experiment, local hot spots could occur along the beam line that would not be measured by our instrumentation. This possibility was investigated with high statistics studies of both the deuterium and helium targets at most of the beam energies used in the experiment, by measuring cross sections at a variety of beam peak currents, repetition rates, and spot size at the target.

The density changes were found to depend only on average beam current ($\propto$ repetition rate $\times$ peak current) and were independent of the beam time structure. For each incident beam energy, the electron cross section for the helium and deuterium targets was parametrized as a linear function of beam power. Figure 9 shows the beam-induced density changes in helium along with the parametrization for two beam energies. The density changes observed had a slope of approximately 2% per μA, and were approximately independent of beam energy. Similar studies and parametrization were done in the case of deuterium.

As an additional check on density corrections, deuterium and helium cross section data were obtained at each kinematic point, with at least two beam pulse repetition rates. A linear parametrization with the slope constrained to be the observed 2% per μA (for He) fitted the cross section very well, and it was used to obtain the cross sections at zero beam current. Corrections for He ranged from 0.2% to 6.7%, and were typically 3%. Corrections for deuterium ranged from 0.1% to 0.9%. We estimate the error to the correction to be about one-third of its value.

2. Empty cell subtraction

The contributions from the Aluminum end caps of the long targets were subtracted from the measured full-target cross sections using cross sections measured in an identical geometry with the empty cells. The contributions were about 1.7% in the case of deuterium and 10.0% in the case of helium.

3. Frame correction

Solid targets were held in a thick frame from which beam halo could scatter. To measure the event yield from this source of background, an empty frame target was used. The contributions from the frame were either negligible (below 0.1%) or amounted to a few tenths of one percent for most of the kinematic points and

solid targets. However, a correction as high as 1.7% was applied for iron at the kinematic point, with $x = 0.3$, $Q^2 = 5$ (GeV/c)^2 and $\epsilon = 0.473$. Data for this kinematic point were taken early in the experiment, when the accelerator had difficulties delivering a stable beam.

4. Charge symmetric processes

Contributions to the scattered electron flux from processes other than electron scattering were a potential source of background. The only significant sources are charge symmetric processes such as neutral pion electroproduction followed by the decay $\pi^0 \rightarrow \gamma + e^+ + e^-$ and $\pi^0 \rightarrow \gamma + \gamma$ followed by $\gamma +$ nucleus $\rightarrow e^+ + e^-$. A previous experiment [36] showed that positron yields with incident electrons, and electron yields with incident positrons, were equal within the experimental accuracy of a few percent. This implies that charge symmetric processes account for at least 95% of the possible background. The electron background flux was determined by reversing the spectrometer polarity and detecting the positrons at the same values of θ and $|P_0|$ as for electrons. The charge symmetric background was largest at low values of x—a maximum of 10% for deuterium at the point with $x = 0.089$ and $Q^2 = 2.0$ (GeV/c)^2—and it was negligible (below 0.1%) at most other kinematic points. The errors on the charge symmetric measurement are primarily statistical. A residual systematic uncertainty estimated to be typically $\pm 0.2\%$ cancels in the ratio of cross sections of different targets.

5. Radiative corrections

Cross sections measured in electron scattering have large contributions from processes other than the one photon exchange Born diagram. The higher order contributions include: internal and external Bremsstrahlung from either the incoming or outgoing electron or from the struck quark, vacuum polarization of the

exchanged photon, photon exchange between the incoming and outgoing electron, two photon exchange with the struck quark, as well as multiple photon emission. These are mostly, in principle, calculable in QED. External radiative effects are the energy loss in the target by the incident electron through Bremsstrahlung before and after scattering. Internal radiative effects are all the possible processes at the struck nucleus aside from the Born diagram. The measured cross sections were radiatively corrected using the exact method of Bardin and collaborators [37] for the internal corrections and the method of Mo and Tsai [38] for the external corrections, in a manner recently developed [39] for SLAC experiments. The internal corrections included vacuum polarization due to electron, muon, tau, and quark loops, as well as higher order electromagnetic corrections and the effects of weak interactions. The results of Bardin's method were compared to an updated version [39] of the exact internal corrections of Tsai. The agreement was better than 1%.

The external corrections were performed using Tsai's exact integrals over the energy loss and internally corrected cross section. To make the calculations feasible, the internal corrections in the triple integral were approximated using the Mo–Tsai (MT) equivalent radiator and angle peaking approximation (but not the energy peaking approximation). The effects of this approximation were cancelled by normalizing the internal plus external corrections using the equivalent radiator method to the internal corrections calculated using both the exact and approximate methods according to

$$\sigma = \sigma_{\mathrm{MT}}^{\mathrm{internal+exact}} \cdot \left(\frac{\sigma_{\mathrm{exact}}}{\sigma_{\mathrm{MT}}} \right)^{\mathrm{internal}} .$$

These external corrections were tested by comparing the final radiatively-corrected cross sections using targets of 2%, 6%, and 12% radiation-length thicknesses. The ratios of cross sections obtained, shown in Fig. 10, are consistant with unity within

the errors of a couple of percent, indicating the external corrections are also accurate to within 1%.

The external radiative corrections depend on the material that the incident and final electrons traverse. The deuterium, helium, and empty cells thicknesses are given in Table 1, while the thickness of the solid targets are given in Table 2. Besides the targets, the incident beam traversed two planes of wire arrays (each equivalent to 0.00036-r.l. thick) and an aluminum 6061 window, 0.0028-cm thick (0.00032 r.l.), which separated the scattering chamber vacuum from the beam line vacuum. A scattered particle, on its way towards the 8 GeV/c spectrometer, traversed the scattering chamber window [aluminum 6061, 0.0313-cm thick (0.00361 r.l.)], a 31 cm air gap (0.00259 r.l.), and the 8 GeV/c spectrometer entrance window [aluminum 6061, 0.0254-cm thick (0.00293 r.l.)].

Three distinct reactions contribute to the radiative corrections: (a) the radiative tail from elastic electron-nucleus scattering, (b) the radiative tail from quasi-elastic electron-nucleon scattering, and (c) processes in the inelastic continuum.

To calculate the inelastic radiative corrections, a knowledge of the cross sections for all kinematically-allowed lower values of incident energy E and all kinematically-allowed higher values of E' is required. For the inelastic deuterium cross section, we used a global parametrization [21] of previous measurements at SLAC. This model is within a few percent of the best model [40–42] recently available, and the deviations contribute negligibly to the radiative corrections. Inelastic model cross sections for heavier nuclei were obtained as the product of the deuterium model times a factor that accounted for differences in the number of nucleons, nonisoscalar targets, and the EMC effect.

For quasi-elastic scattering, we have used the elastic nucleon scattering cross section model of Gari and Krumpelmann [43] for the magnitude and y-scaling [44]

for the shape. For the elastic electron nucleus cross sections, we have used the models given in Stein et al. [15].

The Z-dependent correction for the nuclear Coulomb field was not applied, but has been calculated [45,46] to be less than 1.5% for Au over our kinematic range.

The radiative corrections were nearly identical for different targets of the same thickness in radiation lengths, except for the deuterium and helium targets, where geometrical effects introduced differences of up to 3%. The contributions from the radiative quasi-elastic tails to the cross sections are typically a few percent, but rise up to a maximum of 10% for the 2% radiation length thick targets at x=0.089 and $Q^2 = 2$ (GeV/c)^2. The contributions from the radiative elastic tails to the cross sections are typically less than 0.1% of the cross sections, but rise up to a maximum of 10% at the same kinematic point.

We estimate an uncertainty of 1% due to radiative corrections. It is likely that this uncertainty is somewhat correlated for neighboring kinematic points. Nevertheless, it is included in the point-to-point systematic errors for the cross section. Since these corrections are very similar for different targets an overall normalization of 0.5% was assigned for the target ratios and 0.4% for target-to-target cross sections.

IV. RESULTS AND COMPARISONS TO MODELS

A. Cross sections

Differential cross sections per nucleon (cross section per nucleus divided by atomic number A) were calculated [in picobarns/(sr·GeV)] for each target in a kinematic point according to

$$\sigma^A \equiv \frac{d^2\sigma}{d\Omega dE'} = \frac{N \cdot F_a \cdot C}{0.6023 \cdot Q \cdot \rho \cdot (\Delta\Omega\Delta E')} , \qquad (8)$$

where N is the number of electrons scattered into the acceptance region $\Delta\Omega\Delta E'$ (in msr-GeV), Q is the number of incident electrons (in units of 10^{15}), and ρ is the target thickness (in gm/cm^2). The constant 0.6023 accounts for Avogadro's number and the various units used. C is the product of corrections for radiative effects, over one-per-pulse, electronic dead time, and detector efficiencies, as discussed in Sec. III. The factor F_a corrects for the nonlinear kinematic variation of the cross section across the asymmetric spectrometer acceptance. It is given by

$$F_a = \frac{C_0^R \cdot \sigma_0^{\rm model} \cdot \sum_i (\Delta\Omega\Delta E')_i}{\sum_i C_i^R \cdot \sigma_i^{\rm model} \cdot (\Delta\Omega\Delta E')_i} ,$$

where $\sigma_i^{\rm model}$ is the model cross section, $(\Delta\Omega\Delta E')_i$ is the acceptance and C_i^R is the value of the radiative corrections, all calculated at the center of the $i^{\rm th}$ bin. The factors $\sigma_0^{\rm model}$ and C_0^R represent the value of the model cross section and radiative corrections evaluated at the values of E' and θ at which the cross sections are reported. Corrections ranged from 0.2% at $Q^2 = 2$ (GeV/c)^2, $x = 0.089$ (where the structure function is relatively constant) versus x to 8.9% at $Q^2 = 5$ (GeV/c)^2, $x = 0.7$ (where the cross section is varying rapidly with kinematics) .

The measured cross sections per nucleon for the various targets are listed in Table 5. The sources of systematic uncertainty and their typical magnitudes are listed in Table 6, and were discussed in detail in Secs. II and III. The uncertainties that are not correlated to kinematic setting (point-to-point errors) are listed at the top of the table. The largest uncertainties are associated with the beam energy and angle. These point-to-point errors have been added in quadrature with the statistical errors to form the random error ($\delta^{\rm rnd}$) shown in Table 5. There is an overall systematic error of 2.1% dominated by the spectrometer acceptance. Target length uncertainties (Δ) are common to cross sections measured from the same target, but uncorrelated from target to target. The uncertainties due to radiative

corrections are probably correlated for neighboring kinematic points. The ratio of the deuterium cross sections to a recent [40] parameterization of all SLAC deep inelastic results, which were normalized to SLAC experiment E140 [47] is shown in Fig. 11. The normalization factor of this experiment compared to E140 is $(1.008 \pm 0.004) \times \text{E139} = \text{E140}$.

B. Cross section ratios

Cross sections per average isoscaler nucleon $(\sigma^A)_{\text{is}}$ were obtained from the cross sections per nucleon given by Eq. (8) according to $(\sigma^A)_{\text{is}} = \sigma^A \cdot F_{\text{is}}$. The factor F_{is} adjusted the cross sections to compensate for neutron excess such that $(\sigma^A)_{\text{is}}$ represents the cross section per nucleon of a hypothetical nucleus with equal number (A/2) of protons and neutrons. We have used the ratio of neutron to proton cross sections [21] $\sigma_n = \sigma_p(1 - 0.8x)$ to calculate F_{is}. Cross sections were adjusted by amounts which ranged from negligible (below 0.1%) up to about 10% in the case of Au at $x = 0.8$. We have assigned relative systematic uncertainties to the cross section ratios due to uncertainties in the values of σ_n/σ_p at high x which ranged from below 0.1% up to $\pm 0.7\%$.

The ratios of cross sections per average isoscaler nucleon for heavy targets compared to deuterium, $(\sigma^A/\sigma^d)_{\text{is}}$, are given in Table 7. The systematic errors are itemized in Table 6. Since $\sigma_L/\sigma_T = \{(F_2/2xF_1)\ [(1 + 4M^2x^2)/Q^2]\} - 1$ has been measured [47] to be independent of atomic weight, the ratio of cross sections σ^A/σ^d is the same as the ratio of structure functions F_2^A/F_2^d and F_1^A/F_1^d.

1. Q^2–dependence

These ratios $(\sigma^A/\sigma^d)_{\text{is}}$ are shown in Fig. 12 as a function of Q^2 for He and Au. Also shown are data from the BCDMS experiment [3]. There appears to be no significant Q^2 dependence across the entire kinematic range. For each value

of x, the SLAC data were fit with the linear form $C_1(1 + C_Q \cdot Q^2)$. Figure 13 shows C_Q as a function of x and indicates quantitatively that there is no significant Q^2 dependence. Also shown for Fe and Ca, is the slope obtained combining our data with that of BCDMS [3] and NMC [6], respectively, which also show no Q^2 dependance.

2. *x–dependence*

The cross section ratios $(\sigma^A/\sigma^d)_{\rm is}$, averaged over Q^2, are shown as a function of x in Fig. 14, where each point corresponds to one spectrometer setting. The spectrometer momentum-angle bite at each kinematic point was also partitioned to obtain the ratios of cross sections per nucleon in smaller ("fine") x bins. These ratios, averaged over Q^2, are shown in Fig. 15 and Table 8 as functions of x. Regardless of binning, several trends can immediately be seen. For $x \sim 0.15$ the ratios are a few percent larger than unity for the heavier targets. In the region $0.3 < x < 0.7$ the ratios are less than unity. The deviation from unity is largest for $x \sim 0.7$ and it is larger for the heavier elements. Except for $x > 0.7$, the trend of the data is opposite to that expected from Fermi motion effects [13]. The EMC effect already exists in a nucleus of as low atomic weight as Helium.

Figure 16 compares the results from this experiment to previous SLAC data (systematic error indicated by Δ) from Stein et al. [15] for Be ($\Delta = \pm 3.2\%$), Al ($\Delta = \pm 3.2\%$), Cu ($\Delta = \pm 4.2\%$), and Au ($\Delta = \pm 10\%$), and to data from Bodek et al. [7,8] for Al ($\Delta = \pm 2.3\%$) and Fe ($\Delta = \pm 1.1\%$). More recent results from Dasu et al. [47] are shown for Fe ($\Delta = \pm 1.1\%$) and Au ($\Delta = \pm 1.1\%$). Also shown are the medium x results from CERN by the BCDMS collaboration [2,3] on N ($\Delta \sim \pm$ 1.3%) and Fe ($\Delta \sim \pm$ 1.6%) and by the EMC–NA2′ collaboration [4] on C ($\Delta \sim \pm$ 0.9%) and Cu ($\Delta \sim \pm 0.9\%$). Figure 17 compares this experiment to data taken at CERN by the NMC Collaboration [6] on He, C and

Ca ($\Delta \sim \pm$ 0.9%), and that taken by the EMC–NA28 collaboration [5] on C and Ca ($\Delta \sim \pm 7\%$). We agree to within errors with all other experiments shown. In most cases, our errors are the smallest and define the x-dependence of the EMC effect for $x > 0.1$.

3. A–dependence

Figure 18 shows the ratio $(\sigma^A/\sigma^d)_{\rm is}$ as a function of atomic weight A for two different values of x. The ratio decreases approximately logarithmically up to the highest values of A, showing no saturation effects. Since the ratio is close to unity, $\log(\sigma^A/\sigma^d) \sim 0.43(\sigma^A/\sigma^d - 1)$, and thus the data can be parametrized by $\sigma^A/\sigma^d = C(x) \cdot A^{\alpha(x)}$, as shown by the solid line in the figure. The deuterium point was included in the fit with an error corresponding to the cross section error. The parametrization does not work well at the deuteron (A=2). The values of $\alpha(x)$ and $C(x)$ are listed in Table 9, and the former is plotted in Fig. 19. The χ^2 per degree of freedom is ≤ 1. Also shown in Fig. 19 is the empirical parameterization

$$\begin{aligned}\alpha(x) \;=\; & -.070 + 2.189\,x - 24.667\,x^2 + 145.291\,x^3 - 497.237\,x^4 + 1013.129\,x^5 \\ & -1208.393\,x^6 + 775.767\,x^7 - 205.872\,x^8. \end{aligned} \tag{9}$$

The fit values of C are close to unity everywhere and a good empirical parameterization is

$$\ln C(x) \;=\; .017 + .018 \ln x + .005(\ln x)^2\,. \tag{10}$$

These parameterizations also characterize the NMC data on He, C, and Ca [6] and are only valid in the range $0.01 < x < 0.88$.

The cross section ratios can also be examined as a function of nuclear density ρ as in Fig. 20 and Table 9. Some models, described below, predict that the probability of overlap of nucleons within the nucleus (which is proportional to nuclear density) is related to the EMC effect. The Q^2-averaged ratios, σ^A/σ^d, were

parametrized in terms of average nuclear density by $\sigma^A/\sigma^d = d(x)\,[1+\beta(x)\cdot\rho(A)]$. The average nuclear density was given by $\rho(A) = 3A/4\pi R_e^3$, with $R_e^2 = 5\langle r^2\rangle/3$. The quantity $\langle r^2\rangle$ is the rms electron scattering radius of the nucleus [48]. The values of $\rho(A)$ (in units of nucleons/fm^3) used in the fits were 0.024 for deuterium, 0.089 for He, 0.062 for Be, 0.089 for C, 0.106 for Al, 0.105 for Ca, 0.117 for Fe, 0.126 for Ag, and 0.147 for Au. As seen in Fig. 20, the ratio $(\sigma^A/\sigma^d)_{\rm is}$ is linearly dependent on the density over the entire region measured. The values of $\beta(x)$ and $d(x)$ are given in Table 9. The average χ^2 per degree of freedom is about 0.8.

4. Effect in deuterium

Since the EMC effect is seen in σ^{He}/σ^d it is possible that even deuterium has nuclear effects beyond those expected from Fermi momentum. Frankfurt and Strikman [49] suggested that the structure functions for nuclei divided by that for nucleons differed from unity by an amount proportional to the nuclear density. This implies

$$\frac{(F_2^d/F_2^N)-1}{(F_2^A/F_2^N)-1} = \frac{\rho^d}{\rho^A} \quad , \tag{11}$$

where $F_2^N = (F_2^p + F_2^n)/2$ for free nucleons and F_2^A and F_2^d are per isoscaler nucleon. This leads to

$$\frac{F_2^d}{F_2^N} \sim 1 + \frac{(F_2^A/F_2^d)-1}{(\rho^A/\rho^d)-1} \quad . \tag{12}$$

The value of F_2^d/F_2^N averaged over all our measured A at each value of x is plotted in Fig. 21 and listed in Table 10. Within the framework of this model, deuterium has a significant EMC effect, especially in the region near $x \sim 0.6$. At the highest value of x, Fermi motion causes F_2^d/F_2^N to increase as expected. Within the context of this model, the free neutron structure function can be extracted [42] from measurements on deuterium, hydrogen, and heavy nuclei without resort to Fermi smearing models.

The free neutron cross section might also be extracted by extending the nuclear density model and using only heavy nuclear targets. The results using our data from Be and C [50] are consistant with the other methods, but have larger statistical errors.

In conclusion, the data is described equally well by a parametrization in terms of nuclear weight or in terms of nuclear density. The data do not directly correlate with binding energy per nucleon, which peaks around Fe, since the measured $(\sigma^A/\sigma^d)_{\rm is}$ ratios continue to decrease in the region $0.3 < x < 0.7$ for elements with atomic weight greater than Fe. Although helium has an anomalous binding energy and nuclear density, it appears to be well parametrized by the above two fits.

C. Theoretical models

The EMC effect has been the subject of a large theoretical effort, with many avenues being explored. We limit ourselves here to a brief discussion of representative ideas, and compare them to the results of this experiment. The reader is referred to any of the excellent review articles [49, 51–54] available in the literature for more detailed discussions and lists of references. Based on their main features, we have grouped the models into three broad categories: (a) binding and x-rescaling, (b) pion and $\Delta(1236)$ enhancement, and (c) quark confinement models.

1. Binding and x–rescaling

The aim of this class of models [55–61] is to explain the EMC effect in terms of nucleon-removal energy, relativistic treatment of Fermi motion, and nucleon–nucleon correlations. Most of the models in this category start from the assumption that the structure function of a bound nucleon (F_2^A) is given by the convolution

$$F_2^A(x,Q^2) \;=\; \int_x^{\max} f_N(z,\epsilon)\cdot F_2^N\left(\frac{x}{z},Q^2\right)\,dz\;, \tag{13}$$

where F_2^N represents the free nucleon structure function, and $f_N(z,\epsilon)$ is the spectral function that accounts for the momentum distribution of the nucleon in the nucleus in terms of the fractions of the light-front momentum carried by the nucleon z and its removal energy ϵ. Some further assumptions have to be made about the behavior of F_2^N and f_N, since the nucleons are off mass shell.

Treatment of the nucleon dynamics by simply taking into consideration the nucleon momentum distribution (Fermi motion) produces, for $x \leq 0.6$, only a few percent deviation of $(\sigma^A/\sigma^d)_{\rm is}$ or $(F_2^A/F_2^d)_{\rm is}$ from unity [13], which is contrary to the experimental results. An attempt to improve this situation was made by Akulinichev et al. [55,56], who studied the effects of nucleon Fermi motion and its average removal energy in a Fermi gas model of the nucleus, with no nucleon–nucleon correlation (single particle model). The values of the removal energies used in these calculations were those obtained from early $(e,e'p)$ experiments, using a Hartree–Fock description of the nucleus. They found that the experimental results on the EMC effect could be reproduced by their model, and that this effect was essentially governed by the average nucleon removal energy. However, this model has been criticized [49,62] on the grounds of improper normalization of the spectral function. Inclusion of the proper normalization factor, the so-called flux factor, strongly suppresses the EMC effect predicted by this model [63].

More recently, Ciofi degli Atti and Liuti [59,60] have shown that nucleon–nucleon correlations induced by realistic interactions strongly increase the average value of the nucleon removal energy over those found using a single particle approach (by approximately a factor of 2), again making this class of models a viable explanation of the EMC effect. Figure 22 shows the results of the present experiment compared to this model (dashed dot line). This model fails to reproduce the anti-shadowing near $x \sim 0.15$, as well as the magnitude of the effect at large x.

2. *Pion enhancement models*

In this approach, the EMC effect is due to an enhancement in the nucleus of the pion field associated with the nucleon–nucleon interaction [64,65,70–73]. The structure function of a nucleon bound in a nucleus of atomic weight A is written as

$$F_2^A = \int_x f_N(z)\, F_2^N\left(\frac{x}{y}, Q^2\right) dz + \int_x f_\pi(y)\, F_2^\pi\left(\frac{x}{y}, Q^2\right) dy\,, \qquad (14)$$

where the first integral represents the convolution of the free nucleon structure function F_2^N with its distribution function f_N^A inside the nucleus. Similar meaning applies to the second integral except that pions are considered instead of nucleons. The removal energy ϵ of Eq. (13) could also be included. The presence of n_π^A pions in a nucleus A carrying, on average, a fraction ϵ_π^A of the nucleus momentum per nucleon reduces the momentum fraction carried by the nucleons $\epsilon_N^A = 1 - \epsilon_\pi^A$ and gives rise to the EMC effect at large x.

Figure 22 compares the ratios $(F_2^A/F_2^d)_{\rm is}$ for Al, Fe, and Au predicted by the model of Berger and collaborators(dotted line) [64,65] to the results of the present experiment. In this model, the A-dependence of the EMC effect arises from taking the pion density proportional to nuclear density [74]. The agreement of the model with the data is substantially good for $x > 0.2$. For $x < 0.2$, the ratio predicted by the model increases monotonically above unity due to the enhancement in the number of pions per nucleon (2%, 9%, 10%, and 12% for deuterium, Al, Fe, and Au) required by the model. This enhancement, however, appears to be in contradiction with the recent results of a Drell-Yan experiment [75]. Frankfurt and Strikman [76] have argued that if the parameters of the pion model are adjusted to be consistent with the Drell-Yan process data [75], it would be able to account for less than 20% of the EMC effect at $x > 0.4$.

3. *Quark confinement models*

The EMC effect appears to indicate a softening of the valence quark momentum distributions in nuclei relative to deuterium. Using the uncertainty principle, this would suggest that quarks in nuclei have a sizable probability of being confined in a volume larger than that of a free nucleon.

In the QCD-inspired model proposed by Close and collaborators [66,67,77], the structure function per nucleon of a nucleus of atomic weight A and deuterium are related by a shift in Q^2

$$F_2^A(x,Q^2) \;=\; F_2^d\left[x, Q^2 \cdot \xi_A(Q^2)\right] , \tag{15}$$

where $\xi_A(Q^2) > 1$ is the so-called Q^2 rescaling parameter. Equation (15) has been interpreted as an indication of more efficient gluon radiation for a quark in a bound nucleon than in a free one. The Q^2-dependence of the rescaling parameter is given by

$$\xi_A(Q^2) \;=\; \xi_A(Q_0^2)^{\alpha_s(Q_0^2)\,/\,\alpha_s(Q^2)} , \tag{16}$$

where α_s is the strong coupling constant and Q_0^2 represents the cutoff for perturbative QCD evolution. The authors then assume that $\xi_A(Q_0^2)$ is related to the quark confinement sizes in a bound (λ_A) and unbound (λ_N) nucleon by

$$\xi_A(Q_0^2) \;=\; \left(\frac{\lambda_A}{\lambda_N}\right)^2 . \tag{17}$$

Using a model for the bound nucleon overlap probability, quark confinement sizes are obtained ranging from $\lambda_d = 1.015\ \lambda_N$ to $\lambda_{Au} = 1.196\ \lambda_N$ with $\lambda_{Fe} = 1.153\ \lambda_N$. For the same targets, the values obtained for the rescaling parameter ($Q^2 = 20$) are $\xi_d = 1.07$, $\xi_{Fe} = 2.02$ and $\xi_{Au} = 2.46$. Figure 22 compares the predictions of the model of Close et al. (dashed line) [66–67] for the ratios F_2^A/F_2^d to the results of this experiment. The agreement is good although the

data consistently crosses unity at slightly larger value of x than the model does. The crossing point in the model is determined by the evolution of the structure function. Because $dF_2/d\ln Q^2$ gets larger at low x, the model will not show any antishadowing at small x.

One possible interpretation of the change in quark confinement size calculated in this model is that the bound nucleon size has increased relative to the free one. This interpretation is usually referred to as nucleon swelling. Frankfurt and Strikman [49,76] have argued that (a) such a significant change ($\sim$ 15% in the case of Fe) should also manifest itself in a change of the elastic form factors of a bound nucleon, especially the magnetic one, and (b) that there is no experimental evidence for such a large effect. Constraints on nucleon swelling have also been provided by a recent experiment [78].

Another mechanism proposed to explain the EMC effect is the formation of clusters with six or more quarks [79-83, 68,69]. Quark cluster models were introduced [84] earlier in order to explain the form factors of light nuclei and the production of fast backward particles. In this class of models, the structure function of a bound nucleon (F_2^A) is written as

$$F_2^A = \int_x^A f_N(z)\, F_2^N\left(\frac{x}{z}, Q^2\right)\, dz + \sum_c \int_x^A f_c(z)\, F_2^c\left(\frac{x}{z}\right)\, dz\,, \qquad (18)$$

where F_2^c is the structure function of the clusters, f_c represents their distribution in the nucleus, and the sum extends over all types of clusters included in the model. In quark cluster models, there is considerable freedom in choosing the clusters to be included (clusters of 6, 9 and 12 quarks have been considered), as well as their structure functions and probability distributions.

Figure 22 compares the results of this experiment to the predictions of the 6-quark cluster model proposed by Chemtob and Peschanski (solid line) [68,69].

The agreement is excellent. The clustering probability required to reproduce the data is roughly proportional to $A^{1/3}$ and has values of 10% for Be, 20% for Fe, and 30% for Au.

Fredrikson [85] has considered a model in which a nucleon is mostly in a bound quark-diquark state, with the diquark being a small spin-0 pair of u- and d-quarks. A relation analogous to Eq. (15) is obtained, except that the Q^2-rescaling parameter is given by the ratio of the diquark mean square radius ($\langle R_{dq} \rangle^2$) in a bound nucleon (A) to the one in a free nucleon (N): $\xi_A = \langle R_{dq} \rangle_A^2 \, / \, \langle R_{dq} \rangle_N^2$. Clearly, values of ξ_A similar to those found in the Q^2 rescaling model described above are required to fit the data.

Frankfurt and Strikman [76] have proposed a color screening mechanism to explain the EMC effect. They argue that one of the characteristics of QCD is the dependence of the hadron-hadron interaction on the spatial size of the quark-gluon configurations in the interacting hadrons. Consequently, point-like configurations (PLC) of a size much smaller than the typical nucleon size would have reduced interactions. Frankfurt and Strikman then argue that the configuration of three-valence quarks with no pion field (which are generally assumed to dominate the nucleon structure function F_2 for $x \geq 0.5$) are configurations of a small size that can be treated as PLC. They then show that point-like configurations are suppressed in a bound nucleon relative to a free one. They estimate values of 0.7–0.8 for F_2^A / F_2^d at $x \sim 0.5$–0.6; the effect is proportional to average nuclear density.

4. Summary

It is apparent from previous sections that many theoretical ideas have been put forward to explain the EMC effect. The number of specific implementations of these ideas is quite large, with over a hundred articles published on the subject.

There are, however, questions about the formalism employed in some of these models that need to be understood; for example, the applicability of the convolution expression used by several of the proposed models has been questioned [77].

Most of the models proposed are able to fit the data from the first generation experiments, including the results of this experiment on the A dependence, by proper adjustment of the model parameters. It is up to the next generations of experiments to determine the validity of these models. Some examples are (1) the recent measurement of the antiquark distributions in nuclei through the Drell-Yan process [75] to determine if they are compatible with the expectations of the pion model, and (2) measuring the nucleon structure functions at $x > 1$ to determine if they are compatible with the quark cluster models.

D. Conclusions

Measurements of the cross sections and their ratios for nuclei ranging from deuterium to gold are reported. These data cover the range of Bjorken x from 0.089 to 0.88 and Q^2 from 2 to 15 (GeV/c^2). These measurements provide the first systematic study of the A–dependence of the EMC effect. These results are consistant with those of EMC, BCDMS, and NMC over the entire range of overlap. For x between 0.3 and 0.7, the ratio $(\sigma^A/\sigma^d)_{\rm is}$ is below unity for all targets studied, including ^{4}He, and $(\sigma^A/\sigma^d)_{\rm is}$ decreases logarithmically with A with no saturation. For $x \sim 0.15$, our results rise above unity by few percent. There is no significant Q^2 dependence over the entire x range.

ACKNOWLEDGMENTS

We wish to acknowledge the support of D. Brown, J. Mark, J. Nicol, B. Smith, and the rest of the SLAC staff; valuable discussions with W. Atwood, S. Brodsky, D. Coward, H. DeStaebler, and M. Soldate; and the help of J. Martoff.

This work was supported in part by US Department of Energy contracts DE–AC03–76SF00515 and DE–AC02–76ER13065, and by National Science Foundation Grant PHY 83–40337. One of us (J.G.) was partially supported by Consejo Nacional de Investigaciones Cientificas y Tecnologicas, Venezuela, and one of us (R.M.L-N.) thanks the Centre National de la Recherche Scientifique, France, for its support.

REFERENCES

1. EMC–NA2, J. J. Aubert et al., Phys. Lett. **B123**, 275 (1983).
2. BCDMS, G. Bari et al., Phys. Lett. **B163**, 282 (1985).
3. BCDMS, A. C. Benvenuti et al., Phys. Lett. **B189**, 483 (1987).
4. EMC-NA2′, J. Ashman et al., Phys. Lett. **B202**, 603 (1988).
5. EMC-NA28, M. Arneodo et al., Nuclear Physics **B333**, 1 (1990).
6. NMC, P. Amaudruz et al., Z. Phys. **C51**, 387 (1991).
7. A. Bodek et al., Phys. Rev. Lett. **50**, 1431 (1983).
8. A. Bodek et al., Phys. Rev. Lett. **51**, 534 (1983).
9. R. G. Arnold et al., Phys. Rev. Lett **52**, 727 (1984).
10. G. Gramer and J. Sullivan, *Electromagnetic Interactions of Hadrons*, A. Donnachie and G. Shaw, eds. (Plenum, New York, 1978), Vol. 2, p. 195.
11. A. Mueller, *Quarks, Leptons, and Supersymmetry: Proceedings of the XVIIth Recontre de Moriond, Les Arcs, France, 1982,* Vol. 1, J. Tran Thanh Van, ed. (Editions Frontieres, Gif-sur Yvette, France, 1982) p. 13.
12. L. V. Gribov, E. M. Levin and M. G. Ryskin, Phys. Rep. **100**, 1 (1983).
13. A. Bodek and J. L. Ritchie, Phys. Rev. **D23**, 1070 (1981), and **D24**, 1400 (1981).
14. W. R. Ditzler et al., Phys. Lett. **57B**, 201 (1975).
15. S. Stein et al., Phys. Rev. **D12**, 1884 (1975).
16. R. B. Neal, *The Stanford Two-Mile Accelerator* (Benjamin, New York, 1968).
17. R. C. Walker et al., Phys. Lett. **B224**, 353 (1989).
18. R. G. Arnold et al., Phys. Rev. Lett. **57**, 174 (1986); A. F. Sill et al.; Phys. Rev. **D48**, 29 (1993), and SLAC–PUB –4395 (1992).
19. R. S. Larsen and D. Horelick in *Proceedings of the Symposium on Beam Intensity Measurement,* Daresbury, England, 1968 (Daresbury Nuclear Physics Laboratory, Daresbury, 1968), pp. 260–279.

20. D. Horelick and R. S. Larsen, Stanford Linear Accelerator Center report SLAC–100 (1969).

21. A. Bodek et al., Phys. Rev. **D20**, 1471 (1979).

22. S. Rock et al., Phys. Rev. **D46**, 24 (1992).

23. D. B. Chelton and D. B. Mann, University of California Radiation Laboratory report UCRL–3421 (1956).

24. D. B. Mann, National Bureau of Standards Technical Note 154 (1962).

25. P. N. Kirk et al., Phys. Rev. **D8**, 63 (1973).

26. E. A. Taylor, ed., *SLAC User's Handbook,* Stanford Linear Accerator Center Technical Note SLAC–TN–71–26 (SLAC, Stanford University, Stanford, California 1971), Section D.3.

27. L. Andivahis et al., Stanford Linear Accelerator Center preprint SLAC–PUB–5753 (1992), unpublished.

28. G. Eigen and E. Lorenz, Nucl. Instrum. Methods **166**, 165 (1979).

29. P. Bosted and A. Rahbar, *A Proportional Wire Chamber System for the SLAC 8 GeV/c Spectrometer,* Stanford Linear Accelerator Center Nuclear Physics at SLAC report SLAC–NPAS–TN–85–1,1985; P. Bosted et al., Phys. Rev. **C42**, 38 (1990).

30. J. Gomez, *Shower Counter for the SLAC 8 GeV/c Spectrometer,* Stanford Linear Accelerator Center Nuclear Physics at SLAC report SLAC–NPAS-TN-84-1 (1984).

31. R. F. Oppenheim, Ph.D. thesis, Yale University, New Haven, Connecticut (1982).

32. M. J. Browne et al., Stanford Linear Accelerator Center preprint SLAC–PUB–2494 (1980), unpublished.

33. D. H. Coward et al., Phys. Rev. Lett. **20**, 292 (1968).

34. J. Gomez, Ph.D. thesis, The American University, Washington DC (1987).

35. K. L. Brown et al., Stanford Linear Accelerator Center Technical Note SLAC–TN–64–18 (1964); K. L. Brown et al., Stanford Linear Accelerator Center report SLAC–75, Rev. 3 (1972); K. L. Brown and R. V. Servanckx, in *Proceedings of the 3rd Summer School on High Energy Particle Accelerators, Physics of High Energy Particle Accelerators,* AIP Conference Proceedings 127, Melvin Month, Per F. Dahl, Margaret Dienes, eds. (American Institute of Physics, New York, 1985), p. 62; also Stanford Linear Accelerator Center preprint SLAC–PUB–3381 (1984).

36. L. S. Rochester et al., Phys. Rev. Lett. **36**, 1284 (1976).

37. D. Yu Bardin and N. M. Shumeiko, Dubna Joint Institute for Nuclear Research preprint JINR–P2–10873; A. A. Akhundov, D. Yu Bardin, and N. M. Shumeiko, Sov. J. Nucl. Phys. 26 (6), 660 (1978), and Dubna Joint Institute for Nuclear Research preprint JINR–E2–10205; and A. A. Akhundov, D. Yu Bardin, and W. Lohmann, Dubna Joint Institute for Nuclear Research preprint JINR–E2–86–104.

38. L. W. Mo and Y. S. Tsai, Rev. Mod. Phys. **41**, 205 (1969); Y. S. Tsai, Stanford Linear Accelerator Center preprint SLAC–PUB–848 (1971), unpublished.

39. S. R. Dasu, Ph.D. thesis, The University of Rochester, Rochester, New York (1988).

40. L. W. Whitlow, Ph.D. thesis, Stanford University, Stanford, California, 1990; also Stanford Linear Accelerator Center report SLAC–357 (1990).

41. L. W. Whitlow, Phys. Lett. **B250**, 193 (1990).

42. L. W. Whitlow, Phys. Lett. **B282**, 475 (1992).

43. M. Gari and W. Krumpelmann, Z. Phys. **A322**, 689 (1985).

44. D. B. Day et al., Ann. Rev. Nucl. Part. Sci. **40**, 357 (1990); D. B. Day et al., Phys. Rev. Lett. **59**, 427 (1987); D. B. Day, Nucl. Phys. **A478**, 397c (1988); P. Bosted et al., Phys. Rev. Lett. **49**, 1380 (1982).

45. S. Brodsky and M. Soldate, private communication.

46. E. Calva–Tellez and D. R. Yennie, Phys. Rev. **D20**, 105 (1979).

47. S. Dasu et al., Phys. Rev. Lett. **60**, 2591 (1988).

48. C. W. DeJager, H. De Vries, and C. De Vries, Atomic Data and Nuclear Data Tables **14**, 479 (1974).

49. L. L. Frankfurt and M. I. Strikman, Phys. Rep. **160**, 235 (1988).

50. A. Bodek, S. Dasu, and S. E. Rock, "Study of Nuclear Effects in the Deuteron and Extraction of Neutron to Proton Structure Function Ratio," in *Tuscon 1991, Proceedings of the Intersections Between Particle and Nuclear Physics,* W. Van Oers, ed., AIP Conference Proceedings 243, p. 768; also Stanford Linear Accelerator Center preprint SLAC–PUB–5598 (1991), unpublished.

51. M. Arneodo in *Quest for Links to New Physics,* Proceedings of the 15th International Warsaw Meeting on Elementary Particle Physics, Kazimierz, Poland, 1992, Z. Ajduk, S. Pokorski, and A. K. Wroblewski, eds. (World Scientific, River Edge, New Jersey, 1993); also CERN preprint CERN–PPE/92–113.

52. R. J. M. Covolan, E. Predazzi in *Problems of Fundamental Modern Physics II,* Proceedings of the 5th Winter School on Hadronic Physics, Folgaria, Italy, 1990; R. Cherubini, P. Dalpiaz, and B. Minetti, eds. (World Scientific, Singapore, 1990) p. 85.

53. E. L. Berger and F. Coester, Ann. Rev. Nucl. Part. Sci. **37**, 463 (1987).

54. V. Barone and E. Predazzi, Ann. Phys. **12**, 525 (1987).

55. S.V. Akulinichev, S.A. Kulagin and G. M. Vagradov, Phys. Lett. **158B**, 485 (1985).

56. S. V. Akulinichev et al., Phys. Rev. Lett. **55**, 2239 (1985).

57. B. L. Birbrair, et al., Phys. Lett. **166B**, 119 (1986).

58. C. A. Garcia Canal, E. M. Santangelo and H. Vucetich, Phys. Rev. **D35**, 382 (1987).

59. C. Ciofi degli Atti and S. Liuti, Phys. Lett. **225B**, 215 (1989).

60. C. Ciofi degli Atti and S. Liuti, Phys. Rev. **C41**, 1100 (1990).

61. F. Gross and S. Liuti, Phys. Rev. **C45**, 1374 (1992), and Continuous Electron Beam Accelerator Facility preprint CEBAF–TH–91–19.

62. L. L. Frankfurt and M. I. Strikman, Phys. Lett. **183B**, 254 (1987).

63. G. L. Li, K. F. Liu and G. E. Brown, Phys. Lett. **213B**, 531 (1988).

64. E .L. Berger, F. Coester and R. B. Wiringa, Phys. Rev. **D29**, 398 (1984).

65. E. L. Berger and F. Coester, Phys. Rev. **D32**, 1071 (1985).

66. F. E. Close, R. G. Roberts and G. G. Ross, Phys. Lett. **129B**, 346 (1983).

67. F. E. Close, R. L. Jaffe, R. G. Roberts and G. G. Ross, Phys. Rev. **D31**, 1004 (1985).

68. M. Chemtob and R. Peschanski, J. Phys. **G10**, 599 (1984).

69. M. Chemtob and R. Peschanski, *New Particle Production: Proceedings of the XIXth Rencontre de Moriond, La Plagne, France, 1984* (J. Tran Thanh Van, ed. (Editions Frontieres, Gif-sur Yvette, France,1984) p. 651; also Centre d'Etudes Nucleaires at Saclay preprint SACLAY–Sph–T–84/49 (1984), unpublished.

70. C.H. Llewellyn Smith, Phys. Lett. **128B**, 107 (1983).

71. M. Ericson and A.W. Thomas, Phys. Lett. **128B**, 112 (1983).

72. A.I. Titov, Sov. J. Nucl. Phys. **40**, 50 (1983).

73. M. Ericson and A. W. Thomas, Phys. Lett. **148B**, 191 (1984).

74. B. L. Friman, V.R. Pandharipande and R. B. Wiringa, Phys. Rev. Lett. **51**, 763 (1983).

75. D.M. Alde et al., Phys. Rev. Lett. **64**, 2479 (1990).

76. L. L. Frankfurt and M. I. Strikman, *Modern Topics in Electron Scattering,* B. Frois and I. Sick, eds. (World Scientific, Singapore, 1991) p. 762; University of Illinois at Urbana preprint ILL–(MAR)–91–6 (1991).

77. R. L. Jaffe, F. E. Close and R. G. Roberts, Phys. Lett **134B**, 449 (1984).

78. J. P. Chen et al., Phys. Rev. Lett. **66**, 1283 (1991).

79. C. E. Carlson and T. J. Havens, Phys. Rev. Lett. **51**, 261 (1983).

80. H. Faissner and B. R. Kim, Phys. Lett. **130B**, 321 (1983).

81. H. Faissner et al., Phys. Rev. **D30**, 900 (1984).

82. H. Faissner et al., Phys. Rev. Lett. **54**, 1902 (1985).

83. K. E. Lassila and U. P. Sukhatme, Phys . Lett. **209B**, 343 (1988).

84. H. J. Pirner and J. P. Vary, Phys. Rev. Lett. **46**, 1376 (1981). See also Ref. [49] and references there in.

85. S. Fredrikson, Phys. Rev. Lett. **52**, 724 (1984).

TABLE CAPTIONS

1. Deuterium and ^{4}He target dimensions. Except where otherwise indicated, all dimensions are in radiation lengths (r.l.).
2. Solid target dimensions. All materials had natural isotopic abundance. The quoted material purity is as stated by the manufacturer; they were not measured.
3. Individual wire chamber performance. The wire chamber notation used indicates the type of chamber, wire orientation and position along the incident particle trajectory. For example, a T–type chamber with wire orientation at –30° in the fifth position along the incident particle trajectory is indicated as –T5. The groups/chamber represents the average number of hits per event that a given chamber had while the wires/group represent the average number of wires that went off per hit.
4. Tracking performance. Quantities are the percentage of total number of electron events which have the indicated number of tracks (shown in left column). Entries in different columns are for the specified minimum number of chambers with hits that were required for the tracking algorithm.
5. Cross sections per nucleon (cross section per nucleus divided by Atomic Number A). Values shown should be multiplied by 10^{α} where α is listed for each kinematic point. Errors (δ^{rnd}) are point-to-point systematic added in quadrature with statistical errors. The point-to-point errors include a 1% contribution from the radiative corrections. The systematic error shown as Δ is the target-to-target systematic error dominated by target thickness and including a 0.4% radiative correction uncertainty. The overall systematic error is 2.1% dominated by the spectrometer acceptance.
6. Sources and typical magnitude of the systematic uncertainties, as well as their effects on the cross sections and cross section ratios. The upper half of

the table lists the point-to-point systematic uncertainties. These are added in quadrature with the statistical error to form the random error ($\delta^{\rm rnd}$). The lower half shows the systematic errors which are partly (radiative corrections) or completely correlated between kinematic points.

7. Cross section ratios for individual kinematic points corrected for neutron excess. Errors ($\delta^{\rm rnd}$) are point-to-point systematic added in quadrature with statistical errors. The systematic error shown as Δ is the target-to-target systematic error dominated by the target thickness and including a 0.5% radiative correction uncertainty. There is an overall systematic error of 1.0% dominated by the uncertainty in deuterium target thickness.
8. Cross section ratios averaged over Q^2, corrected for neutron excess and presented in fine x bins. Systematic errors are the same as in Table 7.
9. Fit coefficients versus x. The coefficients are from the fits $(\sigma^A/\sigma^d)_{\rm is} = C(x) \cdot A^{\alpha(x)}$ and $(\sigma^A/\sigma^d)_{\rm is} = d(x)\,[1 + \beta(x) \cdot \rho(A)]$ are shown for both coarse and fine x bins. The fits include $A = 2$.
10. The value of F_2^d/F_2^N obtained from averaging over all measured A using Eq. (12). F_2^N is the average of the free proton and neutron structure function. The combined statistical and systematic errors are shown.

Table 1.

Component	Deuterium	Empty Deuterium	Helium	Empty Helium
Target length (cm)	15.028	14.927	24.875	24.777
Flow separator (Mylar)	0.000177	0.000177	0.000177	0.000177
Cell wall (Al)	0.00132	0.00132	0.00496	0.00484
Target insulation (Mylar)	0.000221	0.000221	0.000221	0.000221
Entrance end cap (Al)	0.000778	0.01068	0.00230	0.01097
Exit end-cap (Al)	0.001152	0.01057	0.00469	0.01105

Table 2.

Material	A	Z	Density (gm/cm^3)	Thickness (gm/cm^2) ± (%)	(r.l.)	Purity (%)
Be	9.0122	4	1.848	1.3815 ± 0.5	0.0212	99.9
C	12.0111	6	2.1917	0.8933 ± 0.5	0.0211	99.9
C	12.0111	6	1.8467	2.5914 ± 0.5	0.0607	99.9
Al	26.9815	13	2.6989	0.5117 ± 0.5	0.0213	99.999
Al	26.9815	13	2.6989	1.4399 ± 0.5	0.0600	99.999
Al	26.9815	13	2.6989	2.8807 ± 0.5	0.1200	99.999
Ca	40.0800	20	1.55	0.9822 ± 0.7	0.0608	99.9
Fe	55.8470	26	7.874	0.2896 ± 1.4	0.0209	99.9
Fe	55.8470	26	7.874	0.8461 ± 0.5	0.0611	99.9
Fe	55.8470	26	7.874	1.6517 ± 0.5	0.1194	99.9
Ag	107.8700	47	10.50	0.5350 ± 1.0	0.0596	99.9
Au	196.9670	79	19.32	0.3951 ± 2.3	0.0612	99.9
Au	196.9670	79	19.32	0.7784 ± 1.3	0.1205	99.9

Table 3.

Quantity	Chamber										Average
	–T1	P2	+T3	P4	–T5	P6	+T7	P8	–T9	P10	
						Data Set 1					
Inefficiency (%)	3.8	6.9	3.7	2.9	2.6	4.1	4.4	1.8	7.1	6.2	4.3
Groups/Chamber	1.63	1.68	1.53	1.64	1.56	1.55	1.43	1.48	1.47	1.47	1.54
Wires/Group	1.18	1.26	1.16	1.32	1.17	1.29	1.16	1.27	1.20	1.17	1.22
						Data Set 2					
Inefficiency (%)	5.3	9.8	1.3	1.2	2.4	7.1	7.2	1.2	4.9	7.4	4.8
Groups/Chamber	1.16	1.14	1.12	1.15	1.17	1.16	1.14	1.16	1.19	1.15	1.15
Wires/Group	1.08	1.09	1.05	1.12	1.09	1.13	1.07	1.13	1.10	1.08	1.09

Table 4.

Tracks Found	Minimum Number of Chambers Required on Track											
	Data Set 1						Data Set 2					
	5	6	7	8	9	10	5	6	7	8	9	10
0	0.4	0.5	0.6	1.1	4.1	22.9	0.4	0.4	0.6	0.8	2.8	18.9
1	95.8	95.7	95.6	95.1	92.7	75.3	94.1	94.1	93.9	93.6	92.5	78.7
2	3.5	3.5	3.5	3.5	3.0	1.7	5.3	5.3	5.3	5.3	4.7	2.4
3	0.3	0.3	0.3	0.3	0.2	0.1	0.2	0.2	0.2	0.2	0.1	0.0

Table 5.

				$[\sigma \pm \delta^{\mathrm{rnd}}] \times 10^{\alpha}$ [pb/(sr · GeV)]				
x	Q^2	ϵ	α	^{2}H (Δ=±1.0%)	^{4}He (Δ=±2.1%)	^{9}Be (Δ=±0.6%)	^{12}C (Δ=±0.6%)	^{27}Al (Δ=±0.6%)
0.089	2.00	0.391	4	1.195 ± 0.020	...	...	...	...
0.130	2.00	0.574	4	1.895 ± 0.031	1.965 ± 0.043	1.948 ± 0.031	...	1.954 ± 0.027
0.140	5.00	0.420	3	3.568 ± 0.086	...	...	...	...
0.220	2.00	0.785	4	3.559 ± 0.056	3.582 ± 0.077	3.527 ± 0.054	...	3.577 ± 0.054
0.220	5.00	0.539	3	3.632 ± 0.056	3.585 ± 0.077	3.593 ± 0.055	3.629 ± 0.048	3.638 ± 0.046
0.300	2.00	0.828	4	3.325 ± 0.052	3.386 ± 0.070	3.308 ± 0.051	...	3.323 ± 0.051
0.300	5.00	0.473	3	1.731 ± 0.027	...	...	...	...
0.300	5.00	0.688	3	4.717 ± 0.073	4.660 ± 0.101	4.611 ± 0.069	4.760 ± 0.074	4.700 ± 0.070
0.300	10.00	0.500	2	9.171 ± 0.155	...	...	...	...
0.400	2.00	0.903	4	4.821 ± 0.074	4.724 ± 0.100	4.534 ± 0.068	...	4.636 ± 0.069
0.400	5.00	0.723	3	3.393 ± 0.046	3.330 ± 0.070	3.231 ± 0.042	3.312 ± 0.040	3.283 ± 0.038
0.400	10.00	0.637	2	9.315 ± 0.139	8.934 ± 0.204	8.749 ± 0.133	...	8.922 ± 0.137
0.500	2.00	0.934	4	5.283 ± 0.080	4.981 ± 0.106	4.911 ± 0.074	...	4.861 ± 0.059
0.500	5.00	0.711	3	1.850 ± 0.028	1.780 ± 0.039	...	...	...
0.500	5.00	0.828	3	3.916 ± 0.052	3.710 ± 0.075	3.661 ± 0.048	3.698 ± 0.049	3.605 ± 0.047
0.500	10.00	0.646	2	5.185 ± 0.090	4.907 ± 0.120	4.750 ± 0.084	...	4.820 ± 0.087
0.600	5.00	0.881	3	3.523 ± 0.048	3.319 ± 0.066	3.199 ± 0.044	3.206 ± 0.041	3.149 ± 0.039
0.600	10.00	0.763	2	4.859 ± 0.077	4.559 ± 0.104	4.317 ± 0.068	4.373 ± 0.071	4.265 ± 0.068
0.600	15.00	0.629	2	1.334 ± 0.022	1.245 ± 0.031	1.160 ± 0.020	...	1.213 ± 0.021
0.700	5.00	0.769	2	7.627 ± 0.122	...	...	...	...
0.700	5.00	0.910	3	2.653 ± 0.043	2.441 ± 0.057	2.313 ± 0.037	2.356 ± 0.036	2.314 ± 0.034
0.700	10.00	0.765	2	2.142 ± 0.040	2.030 ± 0.055	1.909 ± 0.036	...	1.876 ± 0.035
0.800	10.00	0.821	2	1.184 ± 0.025	1.126 ± 0.031	1.079 ± 0.023	...	1.134 ± 0.024

				^{40}Ca	^{56}Fe	^{108}Ag	^{197}Au	
x	Q^2	ϵ	α	(Δ=±0.8%)	(Δ=±1.0%)	(Δ=±1.1%)	(Δ=±2.3%)	
0.089	2.00	0.391	4	...	1.191 ± 0.024	...	...	
0.130	2.00	0.574	4	...	1.966 ± 0.027	...	1.953 ± 0.029	
0.140	5.00	0.420	3	...	3.753 ± 0.084	...	...	
0.220	2.00	0.785	4	...	3.589 ± 0.051	...	3.477 ± 0.061	
0.220	5.00	0.539	3	3.675 ± 0.059	3.649 ± 0.047	3.595 ± 0.063	3.530 ± 0.051	
0.300	2.00	0.828	4	...	3.293 ± 0.048	...	3.162 ± 0.056	
0.300	5.00	0.473	3	...	1.682 ± 0.030	...	...	
0.300	5.00	0.688	3	4.825 ± 0.074	4.704 ± 0.066	4.695 ± 0.077	4.620 ± 0.080	
0.300	10.00	0.500	2	...	8.553 ± 0.191	...	...	
0.400	2.00	0.903	4	...	4.502 ± 0.063	...	4.414 ± 0.075	
0.400	5.00	0.723	3	3.302 ± 0.044	3.236 ± 0.038	3.231 ± 0.045	3.051 ± 0.038	
0.400	10.00	0.637	2	...	8.593 ± 0.124	...	8.376 ± 0.148	
0.500	2.00	0.934	4	...	4.695 ± 0.059	...	4.556 ± 0.063	
0.500	5.00	0.711	3	...	1.649 ± 0.023	...	1.599 ± 0.027	
0.500	5.00	0.828	3	3.663 ± 0.048	3.540 ± 0.044	3.463 ± 0.048	3.405 ± 0.049	
0.500	10.00	0.646	2	...	4.529 ± 0.075	...	4.203 ± 0.093	
0.600	5.00	0.881	3	3.187 ± 0.045	3.035 ± 0.038	2.972 ± 0.044	2.817 ± 0.038	
0.600	10.00	0.763	2	4.337 ± 0.071	4.049 ± 0.061	4.009 ± 0.069	3.786 ± 0.069	
0.600	15.00	0.629	2	...	1.130 ± 0.018	...	1.068 ± 0.023	
0.700	5.00	0.769	2	...	6.302 ± 0.114	...	...	
0.700	5.00	0.910	3	2.344 ± 0.038	2.192 ± 0.033	2.136 ± 0.036	2.036 ± 0.031	
0.700	10.00	0.765	2	...	1.802 ± 0.032	...	1.645 ± 0.038	
0.800	10.00	0.821	2	...	1.091 ± 0.021	...	0.982 ± 0.024	

Table 6.

Source	Uncertainty (±)	$\Delta\sigma$ (±%)	$\Delta(\sigma^a/\sigma^d)$ (±%)
Absolute Beam Energy	< 0.10%	< 0.1–0.5	–
Fluctuations in Beam Energy	0.10%	0.1–0.5	0.1–0.5
Beam angle	0.2 mr	0.3–1.5	0.2–1.0
Beam current (fluctuations)	0.2%	0.2	0.1
Scattered Energy	0.05%	0.1	0.1
Spectrometer Angle	0.10 mr	0.1	–
Acceptance versus p	0.1%	0.1	–
Acceptance versus θ (long targets)	< 0.3%	< 0.3	0.1
Detector efficiency	0.1%	0.1	–
e^+/e^- background	0.2%	0.2%	–
Neutron excess (gold)	< 0.7%		<0.7
Radiative corrections	1.0%	1.0%	–
Total point-to-point systematic		1.2–2.0	0.3–1.3

Source	Uncertainty (±)	$\Delta\sigma$ (±%)	$\Delta(\sigma^a/\sigma^d)$ (±%)
Radiative corrections		0.4	0.5
Beam current (absolute)	0.5%	0.5	–
Target Length deuterium (Δ)	0.9%	0.9	0.9
Solid targets (Δ)	0.5–2.3%	0.5–2.3	0.5–2.3
Acceptance	2.0%	2.0	–
Total absolute errors		2.1–3.1	1.0–2.5

Table 7.

x	Q^2	ϵ	$\left(\frac{\sigma^A}{\sigma^d}\right)_{is.} \pm \delta^{rnd}$ ^{4}He (Δ=±2.2%)	^{9}Be (Δ=±0.7%)	^{12}C (Δ=±0.7%)	^{27}Al (Δ=±0.7%)	^{40}Ca (Δ=±0.9%)	^{56}Fe (Δ=±1.0%)	^{108}Ag (Δ=±1.1%)	^{197}Au (Δ=±2.3%
0.089	2.00	0.391	...	...	...	...	...	0.999±0.019	...	...
0.130	2.00	0.574	1.037±0.022	1.034±0.016	...	1.033±0.014	...	1.041±0.014	...	1.042±0.015
0.140	5.00	0.420	...	...	...	...	...	1.056±0.030	...	...
0.220	2.00	0.785	1.006±0.021	1.002±0.014	...	1.009±0.014	...	1.015±0.014	...	0.996±0.017
0.220	5.00	0.539	0.987±0.021	1.000±0.015	0.999±0.013	1.005±0.012	1.012±0.016	1.012±0.013	1.001±0.017	0.991±0.014
	Average		0.997±0.018	1.001±0.011	0.999±0.013	1.007±0.010	1.012±0.016	1.013±0.010	1.001±0.017	0.993±0.011
0.300	2.00	0.828	1.018±0.020	1.010±0.014	...	1.004±0.014	...	1.000±0.013	...	0.977±0.016
0.300	5.00	0.473	...	...	...	...	...	0.981±0.015	...	...
0.300	5.00	0.688	0.987±0.021	0.993±0.015	1.009±0.015	1.002±0.015	1.023±0.015	1.007±0.014	1.012±0.016	1.006±0.017
0.300	10.00	0.500	...	...	...	...	...	0.942±0.021	...	...
	Average		1.005±0.018	1.002±0.011	1.009±0.015	1.003±0.011	1.023±0.015	0.991±0.009	1.012±0.016	0.991±0.013
0.400	2.00	0.903	0.979±0.020	0.961±0.014	...	0.969±0.014	...	0.947±0.013	...	0.951±0.016
0.400	5.00	0.723	0.982±0.019	0.974±0.010	0.977±0.009	0.975±0.009	0.973±0.011	0.968±0.009	0.975±0.012	0.934±0.010
0.400	10.00	0.637	0.958±0.021	0.960±0.013	...	0.965±0.013	...	0.935±0.012	...	0.934±0.015
	Average		0.975±0.017	0.967±0.008	0.977±0.009	0.972±0.008	0.973±0.011	0.956±0.008	0.975±0.012	0.937±0.008
0.500	2.00	0.934	0.942±0.020	0.956±0.014	...	0.929±0.011	...	0.905±0.011	...	0.906±0.013
0.500	5.00	0.711	0.961±0.020	...	...	...	...	0.908±0.012	...	0.908±0.015
0.500	5.00	0.828	0.946±0.018	0.961±0.010	0.944±0.010	0.929±0.010	0.935±0.010	0.920±0.009	0.912±0.011	0.913±0.011
0.500	10.00	0.646	0.946±0.024	0.943±0.018	...	0.939±0.018	...	0.890±0.016	...	0.852±0.020
	Average		0.949±0.016	0.957±0.009	0.944±0.010	0.930±0.008	0.935±0.010	0.911±0.007	0.912±0.011	0.904±0.009
0.600	5.00	0.881	0.941±0.016	0.941±0.010	0.910±0.008	0.904±0.007	0.904±0.009	0.881±0.007	0.877±0.010	0.852±0.009
0.600	10.00	0.763	0.937±0.020	0.921±0.013	0.900±0.013	0.889±0.013	0.893±0.013	0.853±0.011	0.858±0.014	0.830±0.014
0.600	15.00	0.629	0.932±0.023	0.901±0.015	...	0.920±0.016	...	0.867±0.013	...	0.853±0.018
	Average		0.939±0.016	0.930±0.008	0.908±0.007	0.904±0.007	0.901±0.008	0.874±0.007	0.871±0.009	0.848±0.008
0.700	5.00	0.769	...	...	...	...	...	0.850±0.014	...	...
0.700	5.00	0.910	0.918±0.018	0.911±0.010	0.888±0.008	0.885±0.008	0.883±0.010	0.849±0.008	0.844±0.010	0.830±0.009
0.700	10.00	0.765	0.947±0.026	0.932±0.018	...	0.889±0.017	...	0.866±0.016	...	0.831±0.020
	Average		0.924±0.017	0.915±0.009	0.888±0.008	0.885±0.007	0.883±0.010	0.851±0.007	0.844±0.010	0.830±0.009
0.800	10.00	0.821	0.949±0.024	0.962±0.018	...	0.975±0.018	...	0.954±0.017	...	0.913±0.022

Table 8.

x	$\left(\frac{\sigma^A}{\sigma^d}\right)_{is} \pm \delta^{rnd}$							
	^{4}He (Δ=±2.2%)	^{9}Be (Δ=±0.7%)	^{12}C (Δ=±0.7%)	^{27}Al (Δ=±0.7%)	^{40}Ca (Δ=±0.9%)	^{56}Fe (Δ=±1.0%)	^{108}Ag (Δ=±1.1%)	^{197}Au (Δ=±2.3%)
0.084	...	...	...	...	...	1.015 ± 0.026	...	...
0.094	...	...	...	...	...	0.980 ± 0.027	...	...
0.125	1.030 ± 0.024	1.025 ± 0.017	...	1.036 ± 0.015	...	1.052 ± 0.015	...	1.064 ± 0.017
0.145	1.054 ± 0.039	1.077 ± 0.034	...	1.025 ± 0.028	...	1.022 ± 0.022	...	0.992 ± 0.030
0.205	0.996 ± 0.021	1.006 ± 0.014	1.010 ± 0.017	1.015 ± 0.013	1.040 ± 0.022	1.025 ± 0.013	1.015 ± 0.023	0.994 ± 0.015
0.235	0.997 ± 0.021	0.996 ± 0.015	0.989 ± 0.018	0.999 ± 0.014	0.980 ± 0.022	1.006 ± 0.014	0.986 ± 0.024	0.991 ± 0.016
0.265	1.031 ± 0.030	1.012 ± 0.025	1.068 ± 0.043	1.019 ± 0.025	0.995 ± 0.041	0.990 ± 0.021	0.938 ± 0.042	0.984 ± 0.029
0.295	1.004 ± 0.020	1.003 ± 0.013	1.001 ± 0.018	1.009 ± 0.013	1.037 ± 0.019	0.992 ± 0.010	1.030 ± 0.020	0.993 ± 0.015
0.325	0.991 ± 0.025	0.992 ± 0.020	1.004 ± 0.031	0.975 ± 0.020	0.996 ± 0.031	0.981 ± 0.017	0.998 ± 0.033	0.984 ± 0.024
0.360	0.998 ± 0.021	0.993 ± 0.014	0.987 ± 0.017	0.993 ± 0.013	1.004 ± 0.021	0.972 ± 0.012	1.012 ± 0.023	0.956 ± 0.014
0.400	0.968 ± 0.017	0.957 ± 0.009	0.974 ± 0.011	0.966 ± 0.009	0.966 ± 0.012	0.955 ± 0.009	0.968 ± 0.013	0.930 ± 0.010
0.440	0.949 ± 0.019	0.980 ± 0.014	0.975 ± 0.018	0.959 ± 0.012	0.960 ± 0.019	0.940 ± 0.012	0.957 ± 0.021	0.931 ± 0.014
0.480	0.954 ± 0.017	0.951 ± 0.011	0.953 ± 0.014	0.934 ± 0.010	0.954 ± 0.014	0.917 ± 0.009	0.926 ± 0.015	0.914 ± 0.011
0.520	0.951 ± 0.017	0.955 ± 0.011	0.926 ± 0.012	0.926 ± 0.010	0.912 ± 0.013	0.904 ± 0.009	0.897 ± 0.014	0.892 ± 0.011
0.560	0.943 ± 0.017	0.945 ± 0.011	0.924 ± 0.010	0.923 ± 0.009	0.915 ± 0.012	0.893 ± 0.009	0.891 ± 0.013	0.881 ± 0.011
0.600	0.928 ± 0.017	0.928 ± 0.010	0.905 ± 0.009	0.906 ± 0.009	0.904 ± 0.011	0.869 ± 0.008	0.881 ± 0.012	0.837 ± 0.010
0.640	0.935 ± 0.018	0.917 ± 0.011	0.903 ± 0.010	0.892 ± 0.009	0.895 ± 0.012	0.860 ± 0.009	0.842 ± 0.013	0.846 ± 0.011
0.680	0.917 ± 0.020	0.912 ± 0.013	0.888 ± 0.012	0.876 ± 0.011	0.870 ± 0.015	0.852 ± 0.010	0.842 ± 0.016	0.829 ± 0.013
0.720	0.930 ± 0.022	0.896 ± 0.015	0.861 ± 0.014	0.877 ± 0.012	0.880 ± 0.018	0.846 ± 0.011	0.830 ± 0.019	0.820 ± 0.014
0.760	0.949 ± 0.025	0.931 ± 0.019	0.870 ± 0.020	0.884 ± 0.016	0.890 ± 0.027	0.867 ± 0.015	0.818 ± 0.027	0.817 ± 0.018
0.800	0.927 ± 0.032	0.923 ± 0.027	0.972 ± 0.044	0.957 ± 0.025	0.977 ± 0.058	0.920 ± 0.024	0.941 ± 0.059	0.899 ± 0.030
0.840	0.954 ± 0.054	1.058 ± 0.051	...	1.079 ± 0.051	...	1.040 ± 0.047	...	0.975 ± 0.058
0.880	0.964 ± 0.120	1.135 ± 0.118	...	1.231 ± 0.127	...	1.192 ± 0.116	...	1.099 ± 0.142

Table 9.

x	$C(x) \pm \delta C(x)$	$\alpha(x) \pm \delta\alpha(x)$	$d(x) \pm \delta d(x)$	$\beta(x) \pm \delta\beta(x)$
		Coarse x-bins		
0.130	0.997 ± 0.009	0.0108 ± 0.0034	0.994 ± 0.011	0.397 ± 0.144
0.220	0.998 ± 0.007	0.0020 ± 0.0025	0.998 ± 0.010	0.064 ± 0.115
0.300	1.001 ± 0.008	0.0004 ± 0.0026	1.001 ± 0.011	0.013 ± 0.118
0.400	0.999 ± 0.007	−0.0092 ± 0.0022	1.002 ± 0.010	−0.325 ± 0.100
0.500	1.009 ± 0.007	−0.0234 ± 0.0022	1.016 ± 0.010	−0.814 ± 0.093
0.600	1.008 ± 0.006	−0.0340 ± 0.0020	1.019 ± 0.009	−1.148 ± 0.086
0.700	1.010 ± 0.007	−0.0411 ± 0.0022	1.022 ± 0.010	−1.356 ± 0.086
0.800	1.008 ± 0.010	−0.0149 ± 0.0041	1.011 ± 0.011	−0.509 ± 0.146
		Fine x-bins		
0.125	0.992 ± 0.009	0.0140 ± 0.0036	0.988 ± 0.011	0.507 ± 0.152
0.145	1.002 ± 0.010	0.0049 ± 0.0047	0.999 ± 0.012	0.204 ± 0.189
0.205	0.997 ± 0.008	0.0050 ± 0.0029	0.997 ± 0.011	0.172 ± 0.131
0.235	1.000 ± 0.009	−0.0013 ± 0.0031	1.000 ± 0.011	−0.044 ± 0.131
0.265	1.007 ± 0.010	−0.0028 ± 0.0042	1.004 ± 0.012	−0.041 ± 0.166
0.295	0.999 ± 0.008	0.0023 ± 0.0028	0.999 ± 0.011	0.069 ± 0.125
0.325	1.002 ± 0.009	−0.0044 ± 0.0037	1.004 ± 0.011	−0.160 ± 0.143
0.360	1.004 ± 0.009	−0.0047 ± 0.0030	1.005 ± 0.011	−0.171 ± 0.122
0.400	0.998 ± 0.007	−0.0105 ± 0.0024	1.001 ± 0.010	−0.367 ± 0.103
0.440	1.008 ± 0.008	−0.0147 ± 0.0029	1.013 ± 0.011	−0.530 ± 0.114
0.480	1.006 ± 0.008	−0.0205 ± 0.0025	1.013 ± 0.010	−0.714 ± 0.103
0.520	1.012 ± 0.008	−0.0276 ± 0.0025	1.020 ± 0.010	−0.937 ± 0.099
0.560	1.011 ± 0.007	−0.0289 ± 0.0025	1.020 ± 0.010	−0.984 ± 0.097
0.600	1.010 ± 0.007	−0.0346 ± 0.0023	1.021 ± 0.010	−1.171 ± 0.092
0.640	1.016 ± 0.008	−0.0400 ± 0.0025	1.025 ± 0.010	−1.302 ± 0.093
0.680	1.017 ± 0.008	−0.0442 ± 0.0027	1.027 ± 0.010	−1.427 ± 0.097
0.720	1.017 ± 0.009	−0.0465 ± 0.0030	1.026 ± 0.011	−1.479 ± 0.101
0.760	1.027 ± 0.010	−0.0454 ± 0.0036	1.034 ± 0.011	−1.430 ± 0.115
0.800	1.011 ± 0.010	−0.0219 ± 0.0048	1.015 ± 0.012	−0.734 ± 0.163
0.840	0.994 ± 0.011	0.0090 ± 0.0079	0.995 ± 0.014	0.255 ± 0.304
0.880	0.970 ± 0.014	0.0441 ± 0.0147	0.964 ± 0.019	1.551 ± 0.684

Table 10.

x	F_2^d/F_2^N	Error
0.089	1.000	0.013
0.130	1.012	0.006
0.140	1.014	0.015
0.220	1.001	0.004
0.300	1.001	0.004
0.400	0.990	0.004
0.500	0.979	0.004
0.600	0.969	0.003
0.700	0.962	0.003
0.800	0.986	0.006

FIGURE CAPTIONS

1. Schematic view of the experimental setup in End Station A at SLAC.
2. Schematic view of the target assembly. The liquid deuterium and gaseous ^{4}He targets were cylinders with their major axes parallel to the beam direction. Empty cells, similar in construction to their full counterparts but with thicker end caps, were used to evaluate the contribution to the measured deuterium and helium cross sections from the end caps of the full cells. One of the solid targets positions had no target, and was used to measure the contribution of the frame holding the solid targets.
3. The deuterium and ^{4}He targets. Their major components were: (1) mylar tube, (2) aluminum cell, (3) beam exit end cap, (4) beam entrance end cap, (5) platinum resistors, and (6) vapor pressure bulbs. The deuterium and helium were circulated through the cells. The mylar tube separated the flow of fresh target material from that exposed to the beam. Vapor pressure bulbs and platinum resistors were used to monitor the average temperature of each cell.
4. The SLAC 8 GeV/c spectrometer. The spectrometer consists of three quadrupoles (Q81, Q82, and Q83) and two bending magnets (B81 and B82). Particles scattered into the spectrometer aperture were focused onto a series of detectors located in a shielded enclosure. Concrete shielding, not shown, was placed on top of Q82, B81, B82, and Q83 to minimize the muon background coming straight from the target into the detector enclosure.
5. The 8 GeV/c spectrometer particle detection system. Particles entered from the left. The threshold Čerenkov counter and the segmented lead-glass electromagnetic calorimeter (shower counter) provided particle identification and triggering. Ten planes of wire chambers were used to find the trajectories of the scattered particles, and hence allowed their kinematic reconstruction.

6. Typical electromagnetic calorimeter normalized energy R^{SH} spectra: (a) all events, (b) no Čerenkov signal required (pions), and (c) Čerenkov signal over discriminator threshold required (mostly electrons). The long-dash lines indicate the cut at $R^{SH} = 0.3$, while the short-dash lines indicate the cut of $R^{SH} = 0.74$ used to separate electrons from background. Also shown in (c) as the short dashed curve is the normalized pion spectra used for background subtraction.
7. Typical Čerenkov ADC spectra obtained from the deuterium target at two different kinematic points in this experiment. The arrow indicates the location of the cut imposed on the Čerenkov ADC by requiring events to have a signal above discriminator threshold. The various histograms are discussed in the text.
8. Ratio of the deuterium (a) and He (b) targets acceptance to the thin-target acceptance as a function of angle. The ratios shown are from a Monte Carlo model of the 8 GeV/c spectrometer (see main text). The solid lines represent the parametrization of those ratios. All data in this experiment was taken between 11° and 23°.
9. Beam induced helium density change as a function of average beam current shown for two beam energies. Linear fits to the data are shown as the solid ($E = 17.3$ GeV) and dashed ($E = 21.1$ GeV) lines.
10. Ratios of cross sections obtained from 6%- to 2%-r.l. thick targets of C, Al, and Fe, and for 12%- to 6%-r.l. thick targets of Al, Fe, and Au. Data at the same value of Bjorken x has been displaced slightly in x for easier viewing. Only statistical errors are shown. The results are consistent with unity.
11. Comparison of the deuterium cross sections measured in this experiment to those obtained from a recent parametrization [40] of all SLAC deep-inelastic data. Data at the same value of Bjorken x has been displaced slightly in x

for easier viewing. The combined statistical and point-to-point systematic errors are shown. In addition, there is an overall normalization of 2.5%.

12. The solid circles show $(\sigma^A/\sigma^d)_{\rm is}$ as a function of Q^2 for different x values for Fe and Au targets for this experiment. The errors are statistical and point-to-point systematic added in quadrature. The ratio is for a hypothetical isoscaler nucleus with the same atomic number. The horizontal broken lines represent the Q^2–averaged ratios. Also shown at large Q^2 are data from the BCDMS collaboration [3] with total errors (open circles).
13. The Q^2 dependence of $(\sigma^A/\sigma^d)_{\rm is}$ at various values of x. The slope parameter $d(\sigma^A/\sigma^d)/dQ^2$ is shown for the data for this experiment for Be, Al, Fe, and Au. Also shown for Fe is the slope from the SLAC E140 data [47] and the slope from the data from this experiment (E139) and from BCDMS [3] combined. For Ca the E139 and NMC [6] results have been combined. Points at the same value of x have been slightly offset for clarity.
14. The Q^2-averaged $(\sigma^A/\sigma^d)_{\rm is}$ ratios for isoscaler nuclei as a function of x. Data have been binned by single momentum-angle bite of the spectrometer. The errors shown are the combined statistical and point-to-point systematic errors. In addition, there is a target-to-target systematic error shown in Table 7 and an overall normalization of 1% dominated by the deuterium density.
15. The Q^2-averaged $(\sigma^A/\sigma^d)_{\rm is}$ ratios for isoscaler nuclei as a function of x. The data has been binned in fine-x bins. Errors are the same as in Fig. 14.
16. Comparison of this measurement of $(\sigma^A/\sigma^d)_{\rm is}$ for isoscaler nuclei to other SLAC experiments and to CERN data at moderate values of x. The errors shown for this experiment are the combined statistical and point-to-point systematic. Data for $(\sigma_A/\sigma_d)_{\rm is}$ are shown from SLAC for Be, C, Al, Fe, and Au measured in this experiment (E139), for Be, Al, Cu, and Au reported

by Stein et al. (E61) [15], for Al and Fe reported by Bodek et al. (E87) [7,8], and σ^A/σ^d for Fe and Au reported by Dasu et al. (E140) [47]. Shown from CERN are the $(F_2^A/F_2^d)_{\rm is}$ ratios for nitrogen and Fe measured by the BCDMS collaboration [2,3], and C and Cu measured by the EMC collaboration (NA2′) [4].

17. Comparison of this measurement of $(\sigma^A/\sigma^d)_{\rm is}$ for isoscaler nuclei to measurements from CERN at low values of x. Shown are the $(\sigma^A/\sigma^d)_{\rm is}$ ratios for He, C, and Ca, measured in this experiment and by the NMC Collaboration [6]. Also shown are the C and Ca results of EMC–NA28 [5].

18. The ratios $(\sigma^A/\sigma^d)_{\rm is}$ versus atomic weight A at (a) $x = 0.220$, and (b) $x = 0.600$. The solid lines are a parametrization of the data in terms of $(\sigma^A/\sigma^d)_{\rm is} = C(x)A^{\alpha(x)}$. The errors shown include statistical, point-to-point systematic and target-to-target errors. The overall uncertainty due to the deuterium target is included only at the $A = 2$ point.

19. Atomic weight fit coefficients as a function of x. The $\alpha(x)$ coefficients from the parametrization $(\sigma^A/\sigma^d)_{\rm is} = C(x)A^{\alpha(x)}$ are shown for (a) coarse-x bins, and (b) fine-x bins. The fits include $A = 2$. The curves are a 9-term polynomial fit; see Eq. (9).

20. The ratios $(\sigma^A/\sigma^d)_{\rm is}$ versus nuclear density at (a) x=0.220 and (b) x=0.600. The solid lines represent the parametrization $(\sigma^A/\sigma^d)_{\rm is} = d(x)\ [1+\beta(x)\cdot\rho(A)]$. The errors shown include statistical, point-to-point systematic, and target-to-target errors. The overall uncertainty due to the deuterium target is included only at the $A = 2$ point.

21. The model dependent value of F_2^d/F_2^N extracted from averaging over all measured targets assuming the validity of Eq. (12). F_2^N is the average of the free proton and neutron structure functions. The combined statistical and systematic errors are shown.

22. Comparison of the $(\sigma^A/\sigma^d)_{is}$ ratios for isoscaler targets measured in this experiment to the predictions of various models: Ciofi degli Atti and Liuti (dashed dot line) [59,60]; Berger and collaborators (dotted line) [64,65]; Close et al. (dashed line) [66,67]; Chemtob and Peschanski (solid line) [68,69]. The errors shown are the combined statistical and point-to-point systematic errors. Target-to-target errors (Δ) are listed in Table 7, and the overall normalization is 1%, dominated by the deuterium density.

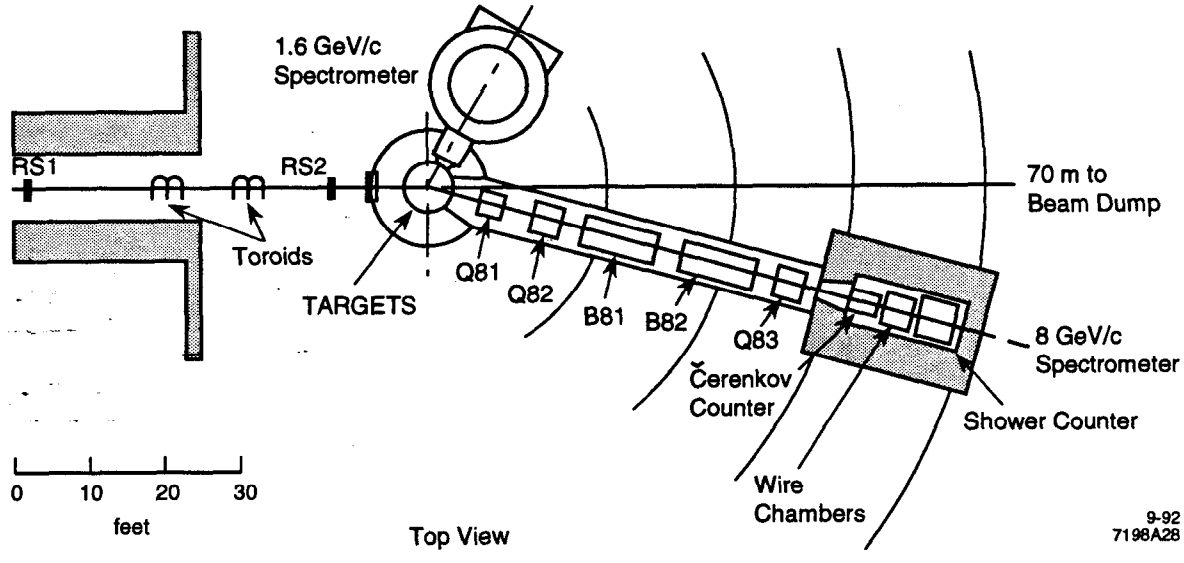
1.6 GeV/c
Spectrometer
RS1
RS2
70 m to
Beam Dump
Toroids
TARGETS
Q81
Q82
B81
B82
Q83
Čerenkov
Counter
8 GeV/c
Spectrometer
Shower Counter
Wire
Chambers
0
10
20
30
feet
Top View
9-92
7198A28

Fig. 1

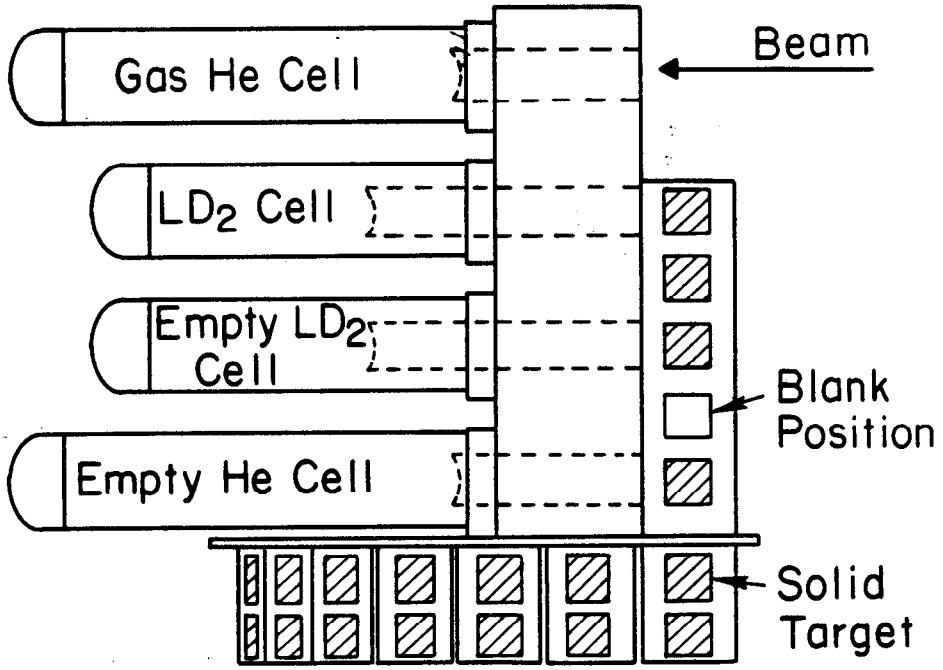

Side View

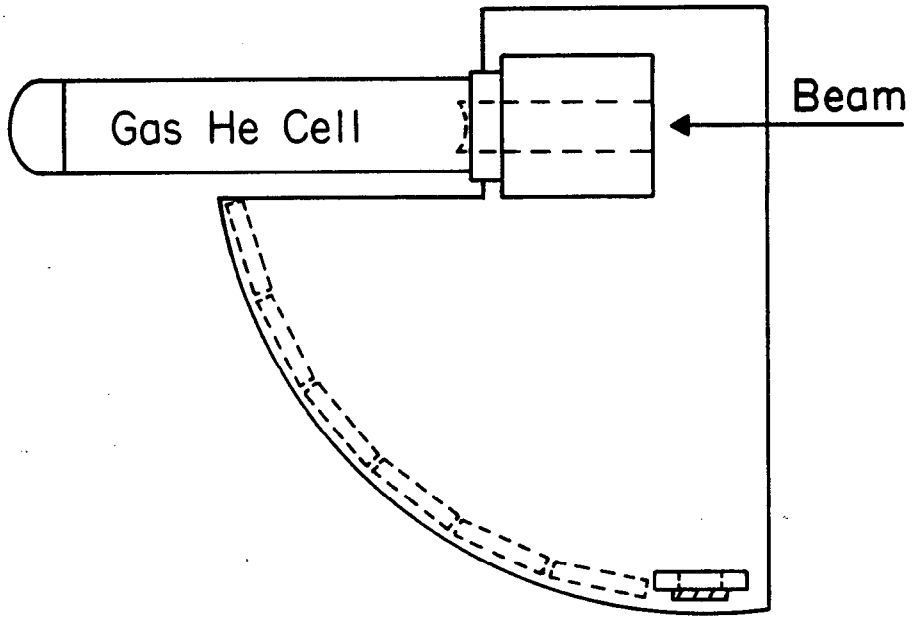

Top View

10-86

5552A5

Fig. 2

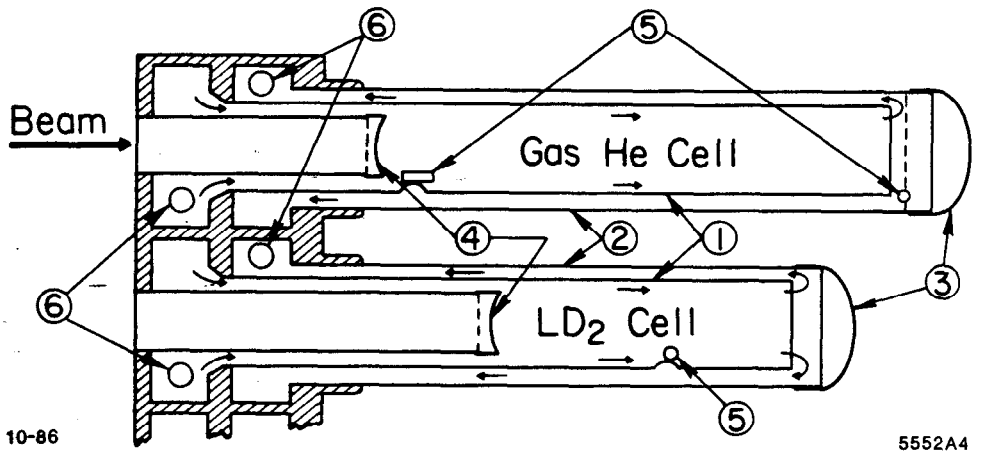

Fig. 3

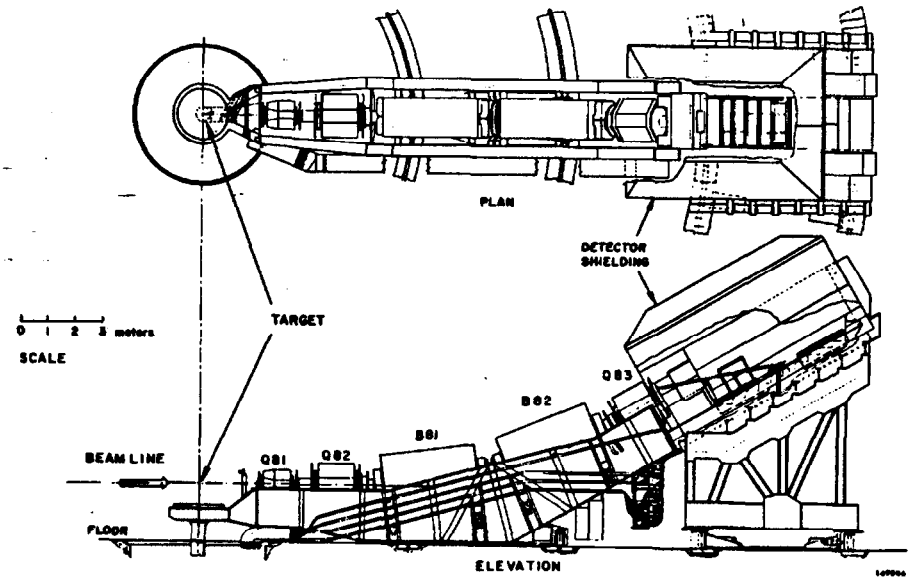
PLAN
DETECTOR SHIELDING
TARGET
0 1 2 3 meters
SCALE
QB3
QB2
QB1
BEAM LINE
QB1
QB2
FLOOR
ELEVATION

Fig. 4

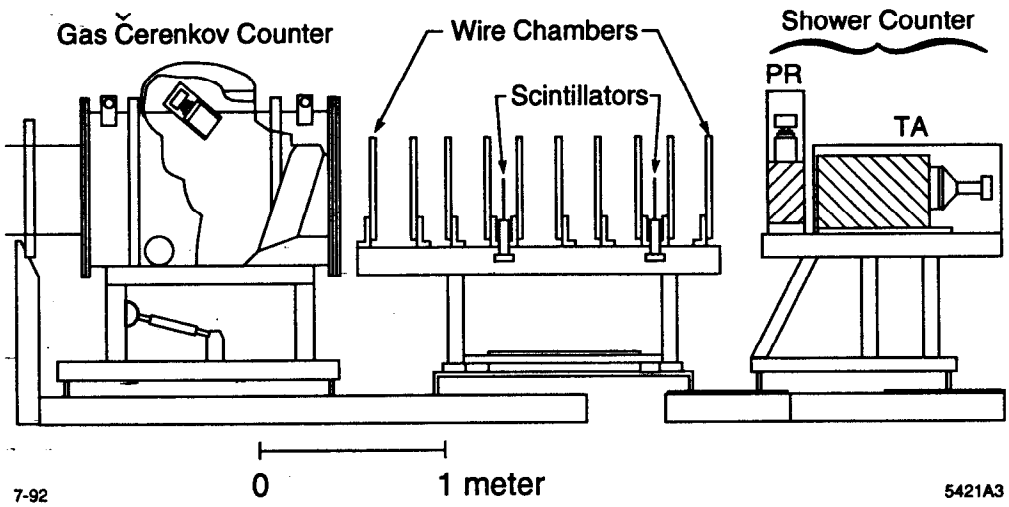
Gas Čerenkov Counter
Wire Chambers
Scintillators
Shower Counter
PR
TA
0
1 meter
7-92
5421A3

Fig. 5

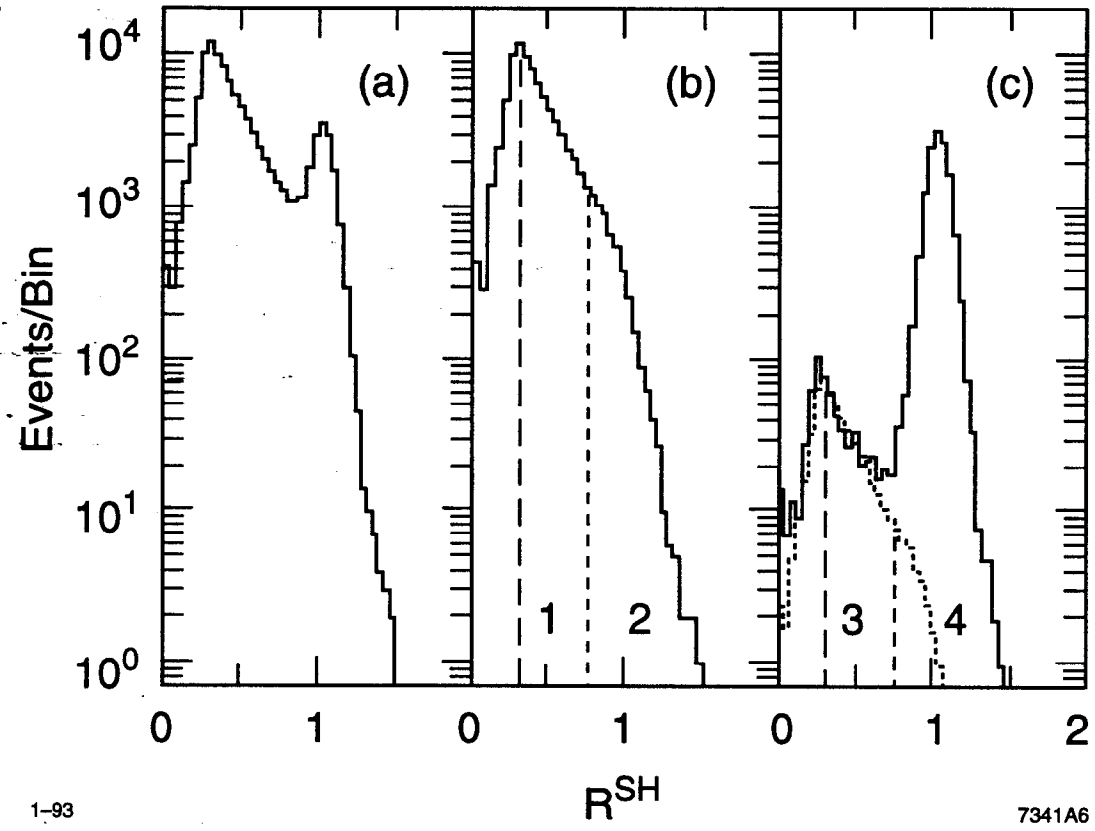
(a)
(b)
(c)
Events/Bin
10^4
10^3
10^2
10^1
10^0
1
2
3
4
0
1
0
1
0
1
2
R^{SH}
1-93
7341A6

Fig. 6

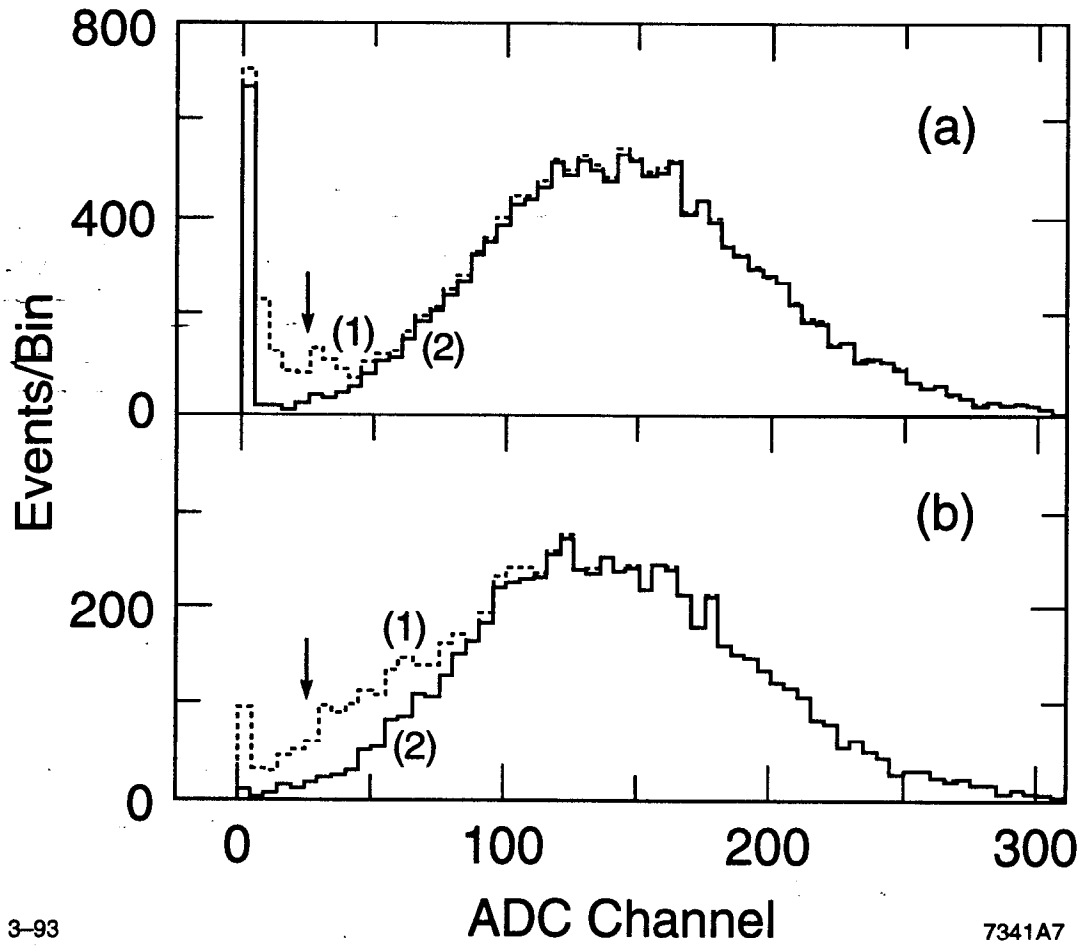
800
400
0
200
0
Events/Bin
(a)
(b)
(1)
(2)
(1)
(2)
0
100
200
300
ADC Channel
3-93
7341A7

Fig. 7

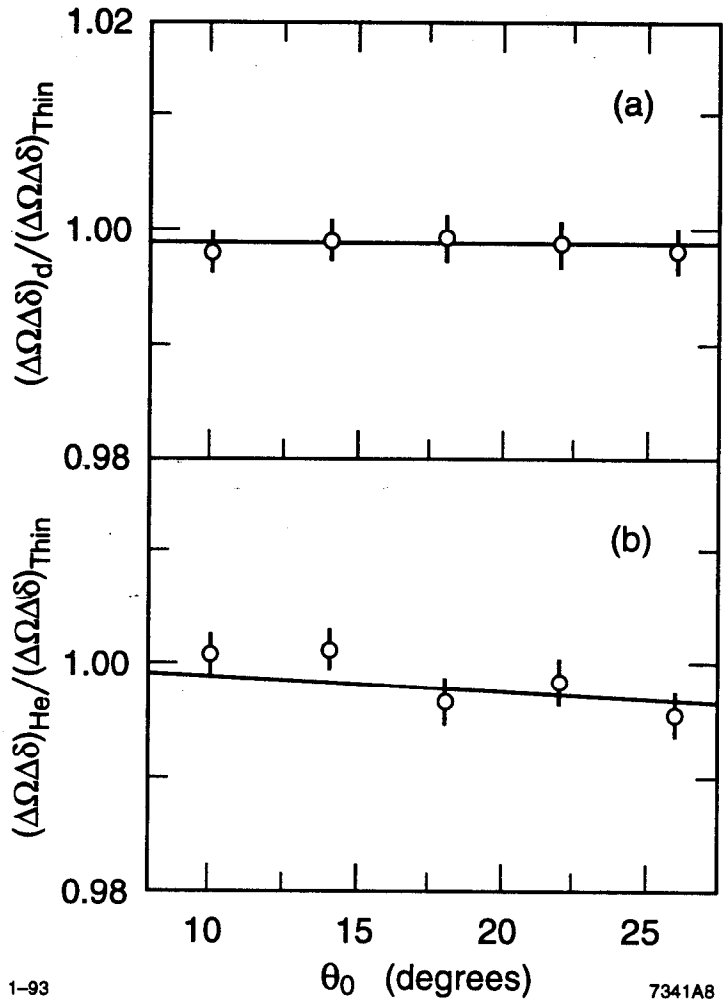
1.02
1.00
0.98
(a)
$(\Delta\Omega\Delta\delta)_d/(\Delta\Omega\Delta\delta)_{Thin}$
(b)
$(\Delta\Omega\Delta\delta)_{He}/(\Delta\Omega\Delta\delta)_{Thin}$
1.00
0.98
10
15
20
25
θ_0 (degrees)
1–93
7341A8

Fig. 8

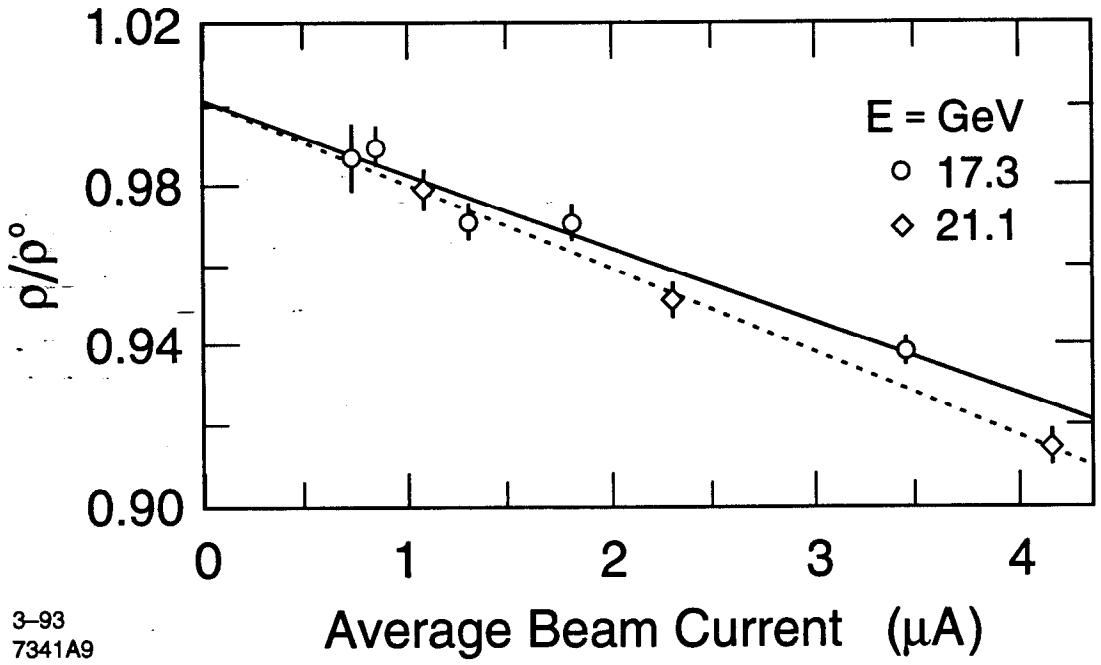
1.02
0.98
0.94
0.90
ρ/ρ°
E = GeV
○ 17.3
◇ 21.1
0
1
2
3
4
Average Beam Current (μA)
3–93
7341A9

Fig. 9

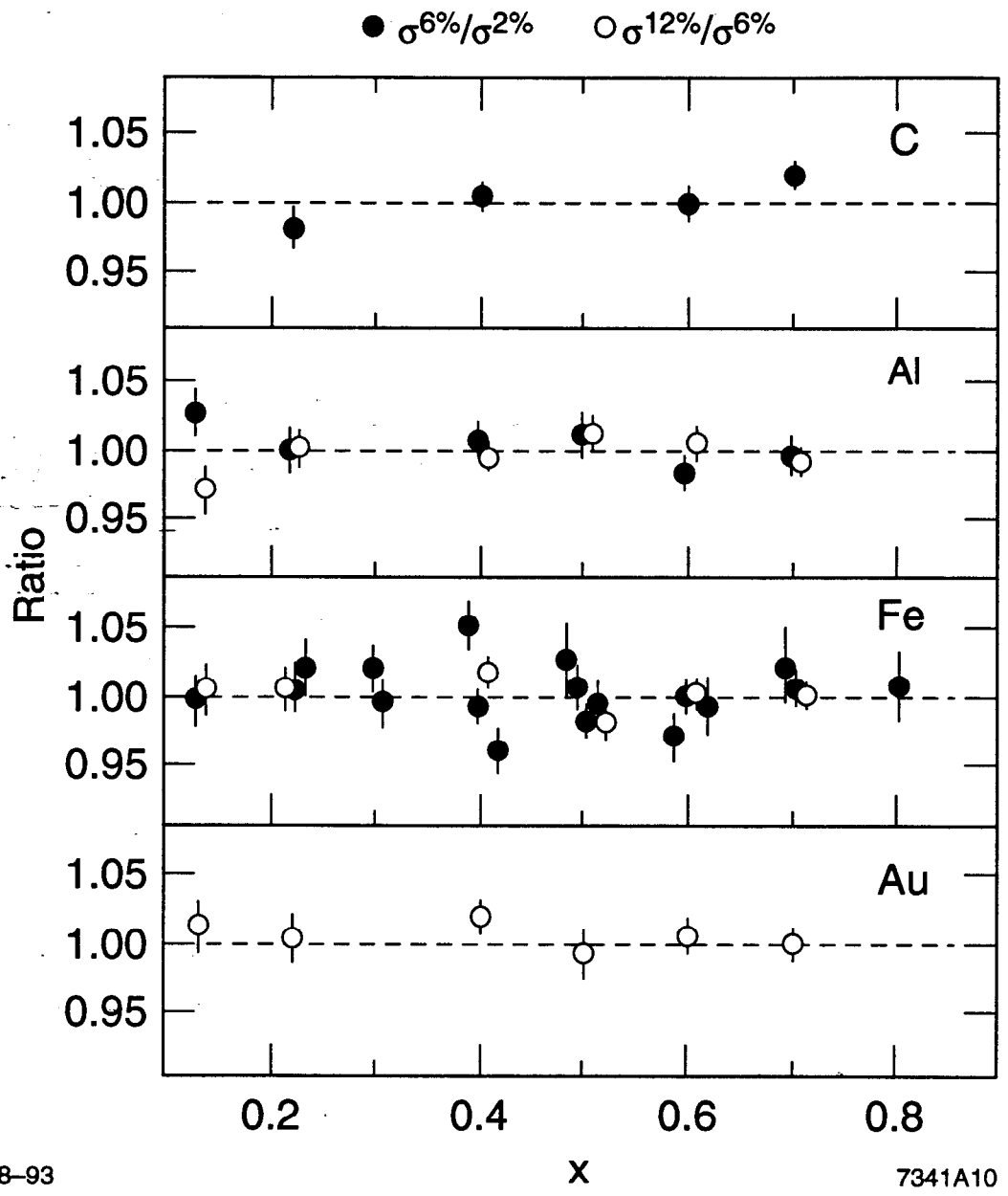

Fig. 10

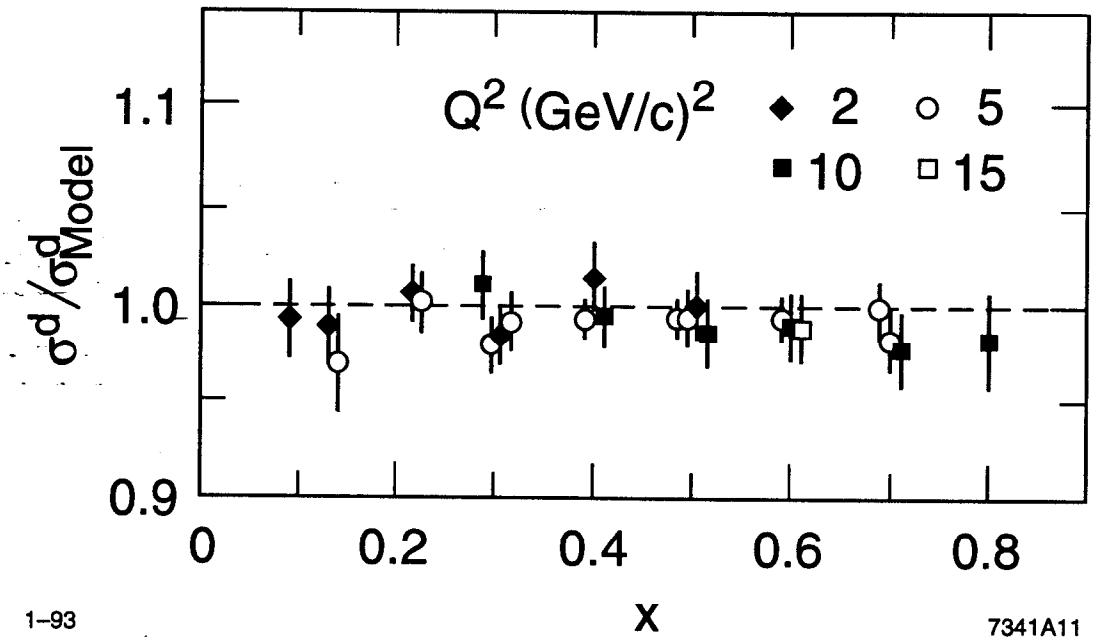
Q^2 (GeV/c)^2
2
5
10
15
$\sigma^d/\sigma^d_{Model}$
1.1
1.0
0.9
0
0.2
0.4
0.6
0.8
x
1–93
7341A11

Fig. 11

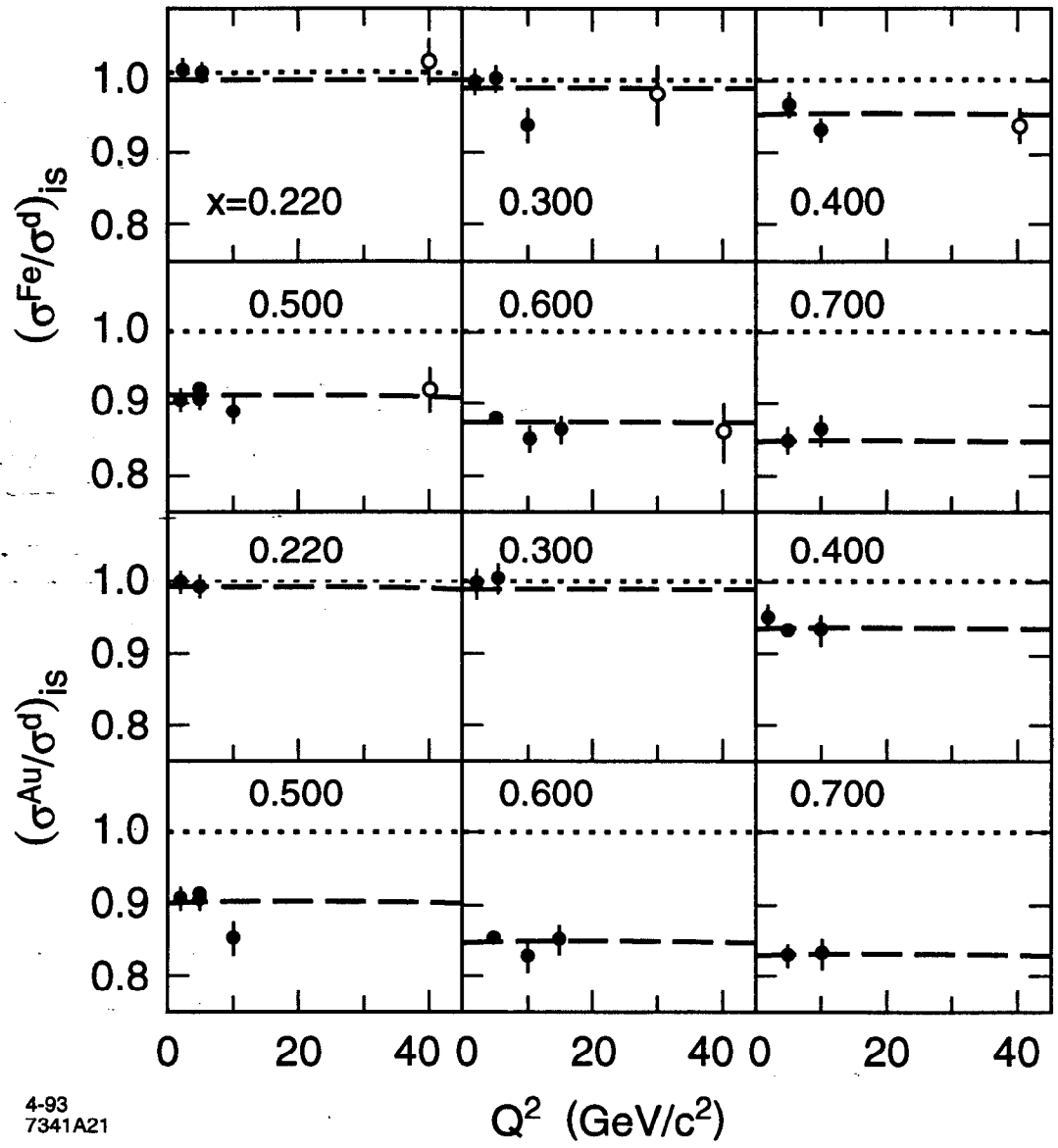
x=0.220
0.300
0.400
0.500
0.600
0.700
0.220
0.300
0.400
0.500
0.600
0.700
1.0
0.9
0.8
0
20
40
$(\sigma^{Fe}/\sigma^{d})_{is}$
$(\sigma^{Au}/\sigma^{d})_{is}$
Q^2 (GeV/c^2)
4-93
7341A21

Fig. 12

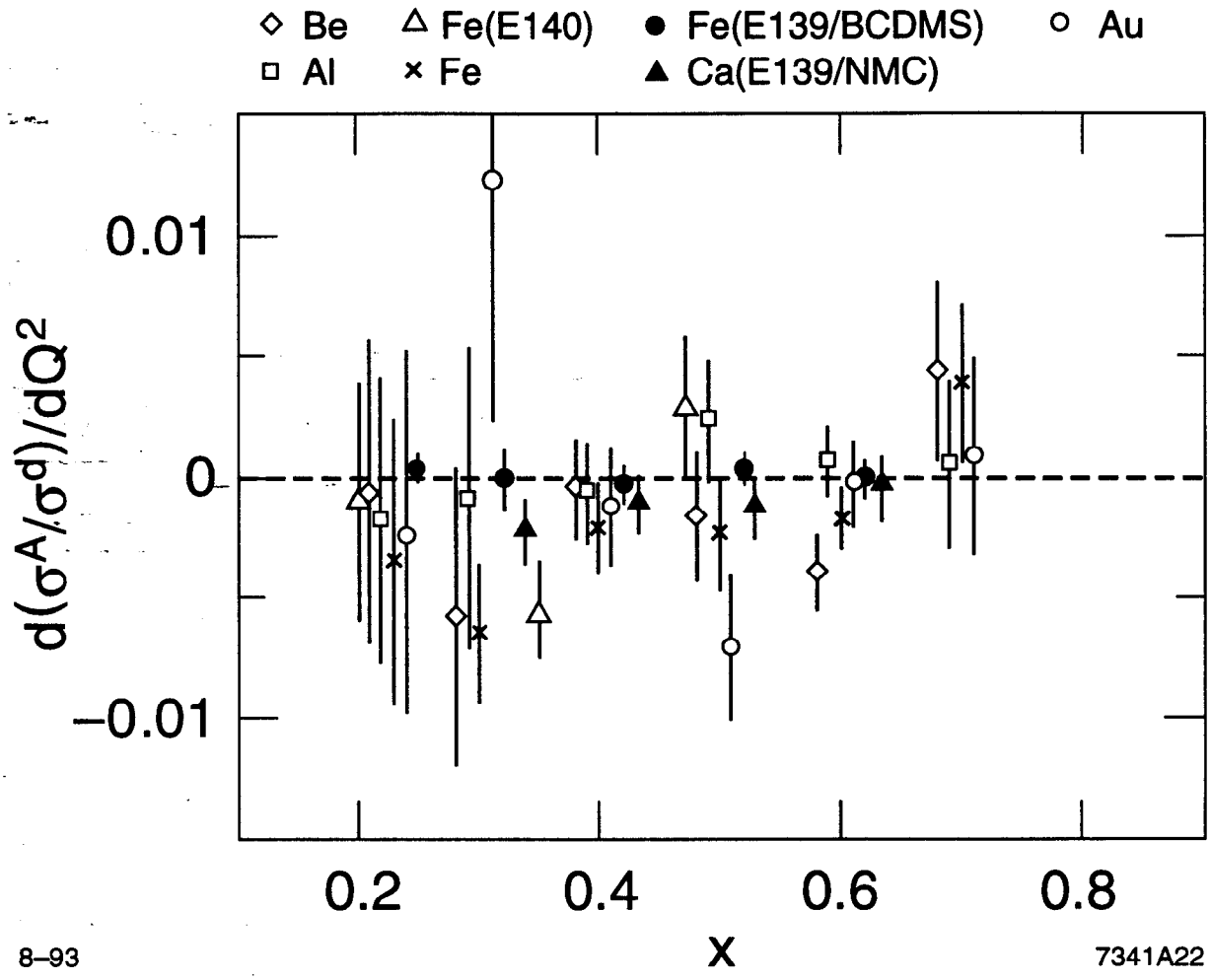
◇ Be
△ Fe(E140)
● Fe(E139/BCDMS)
○ Au
□ Al
× Fe
▲ Ca(E139/NMC)
0.01
0
−0.01
d(σ^A/σ^d)/dQ^2
0.2
0.4
0.6
0.8
x
8–93
7341A22

Fig. 13

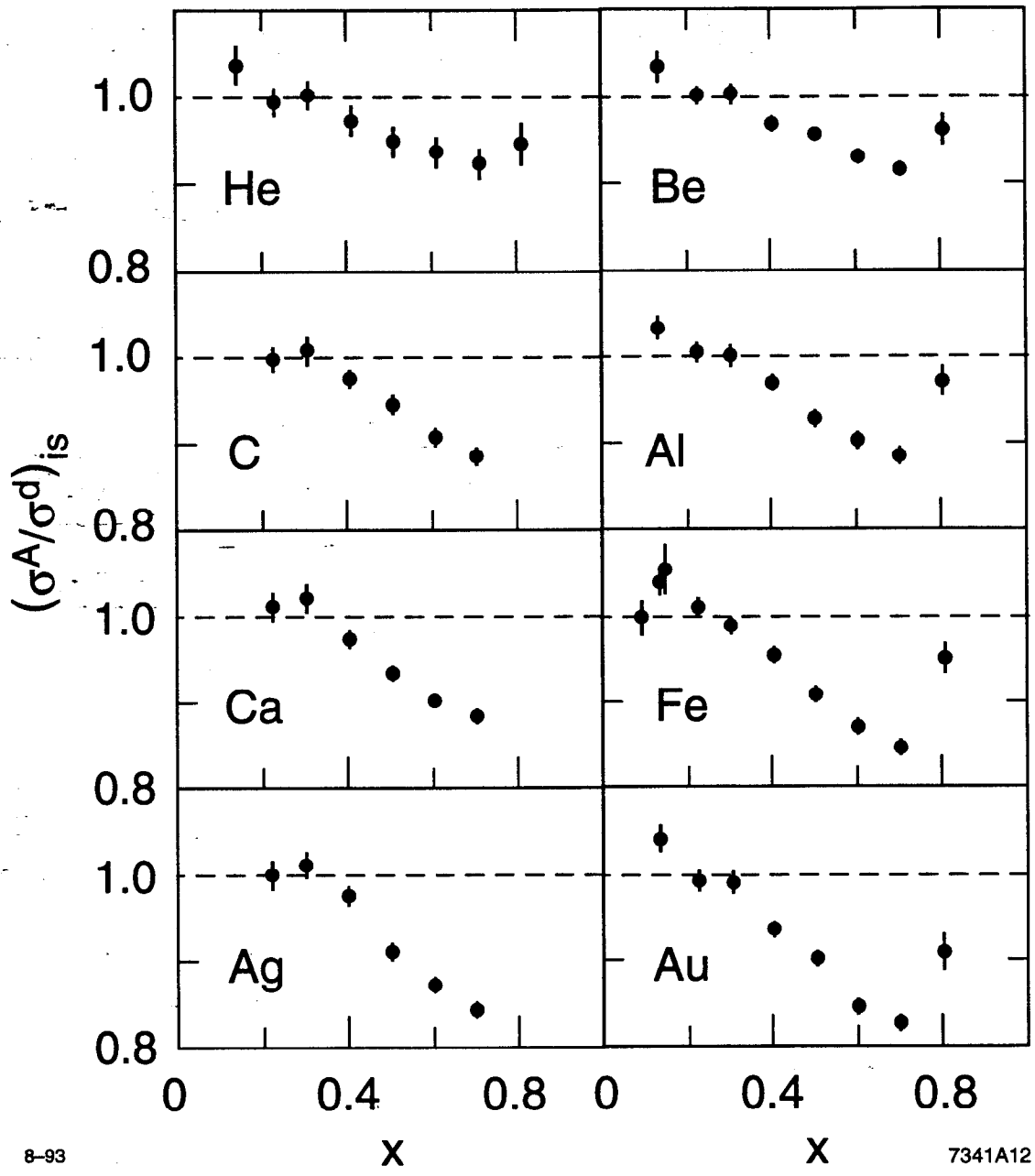

Fig. 14

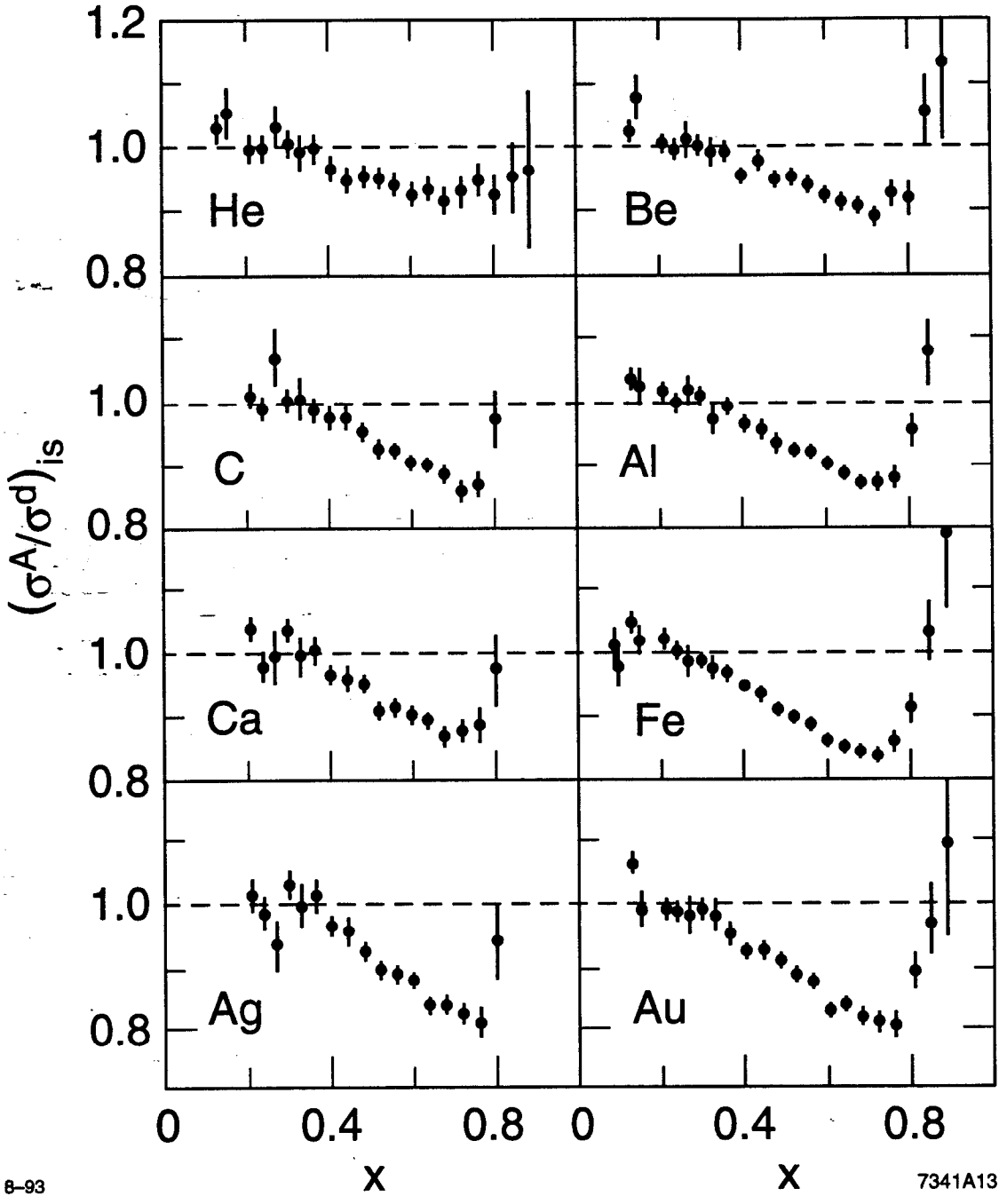
1.2
1.0
0.8
He
Be
C
Al
Ca
Fe
Ag
Au
$(\sigma^A/\sigma^d)_{is}$
0
0.4
0.8
x
8–93
7341A13

Fig. 15

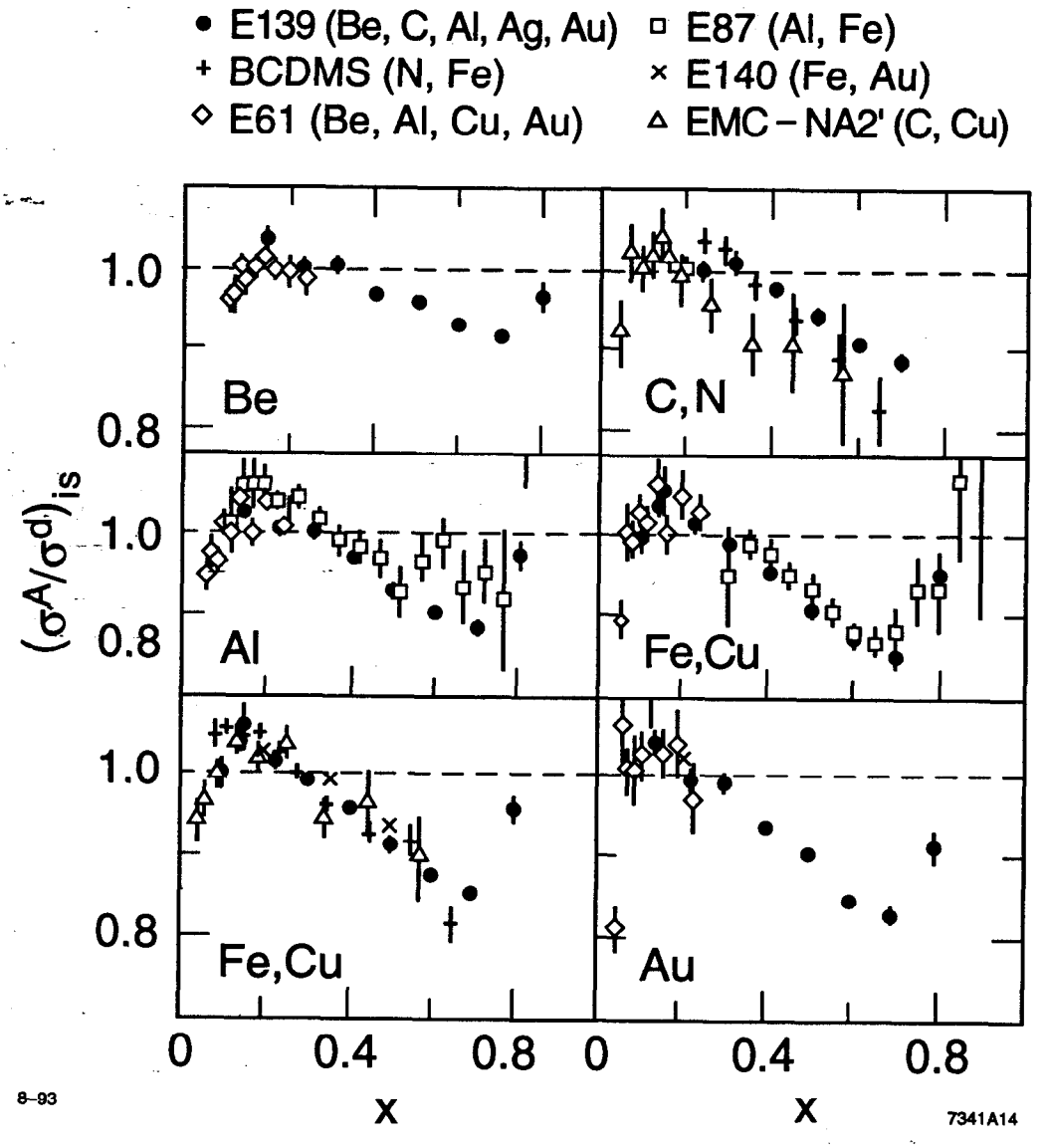
E139 (Be, C, Al, Ag, Au)
E87 (Al, Fe)
BCDMS (N, Fe)
E140 (Fe, Au)
E61 (Be, Al, Cu, Au)
EMC – NA2' (C, Cu)
Be
C,N
Al
Fe,Cu
Fe,Cu
Au
1.0
0.8
0
0.4
0.8
x
$(\sigma^A/\sigma^d)_{is}$
8–93
7341A14

Fig. 16

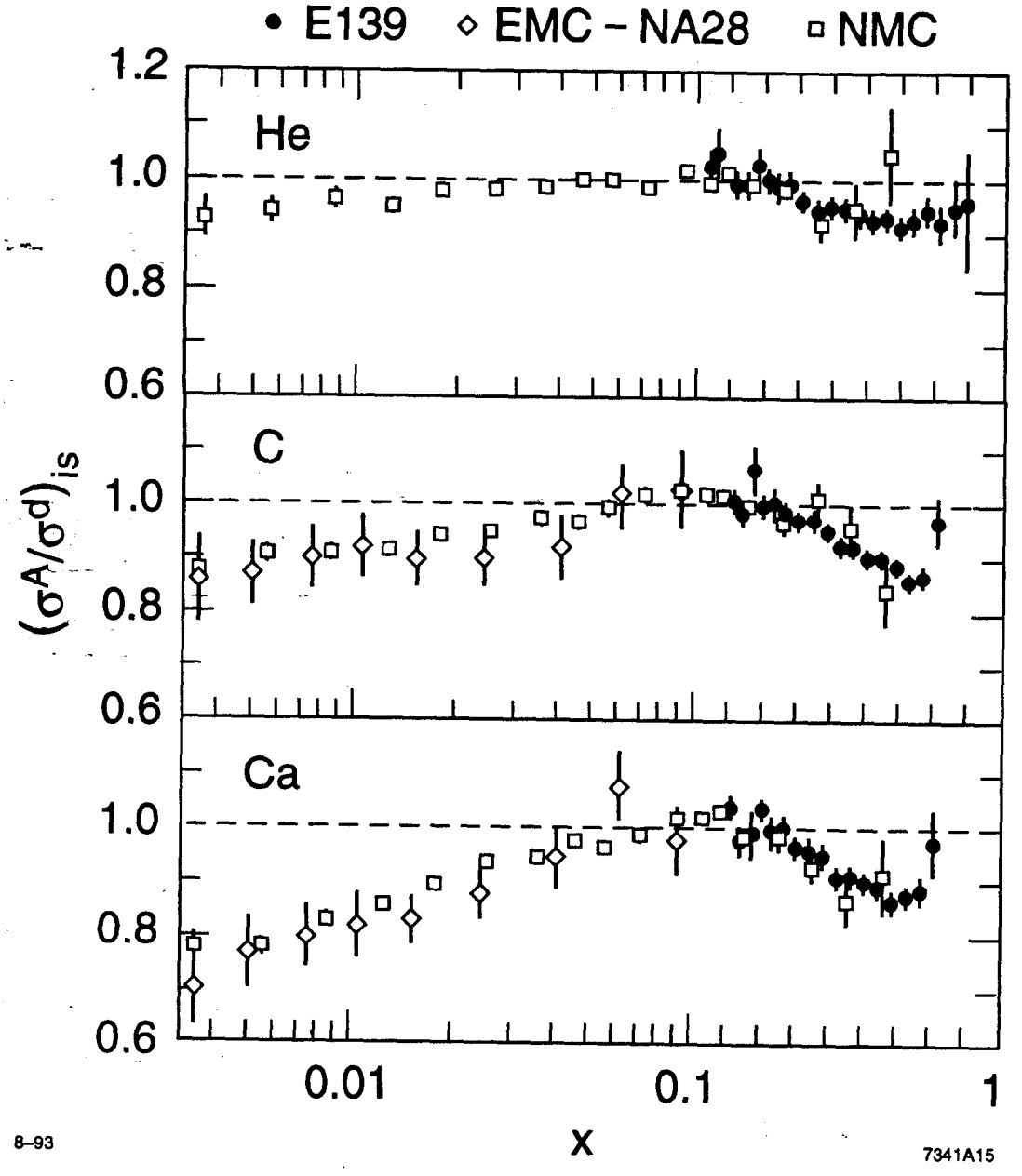
• E139 ◇ EMC – NA28 ▫ NMC
He
C
Ca
1.2
1.0
0.8
0.6
$(\sigma^A/\sigma^d)_{is}$
0.01
0.1
1
x
8–93
7341A15

Fig. 17

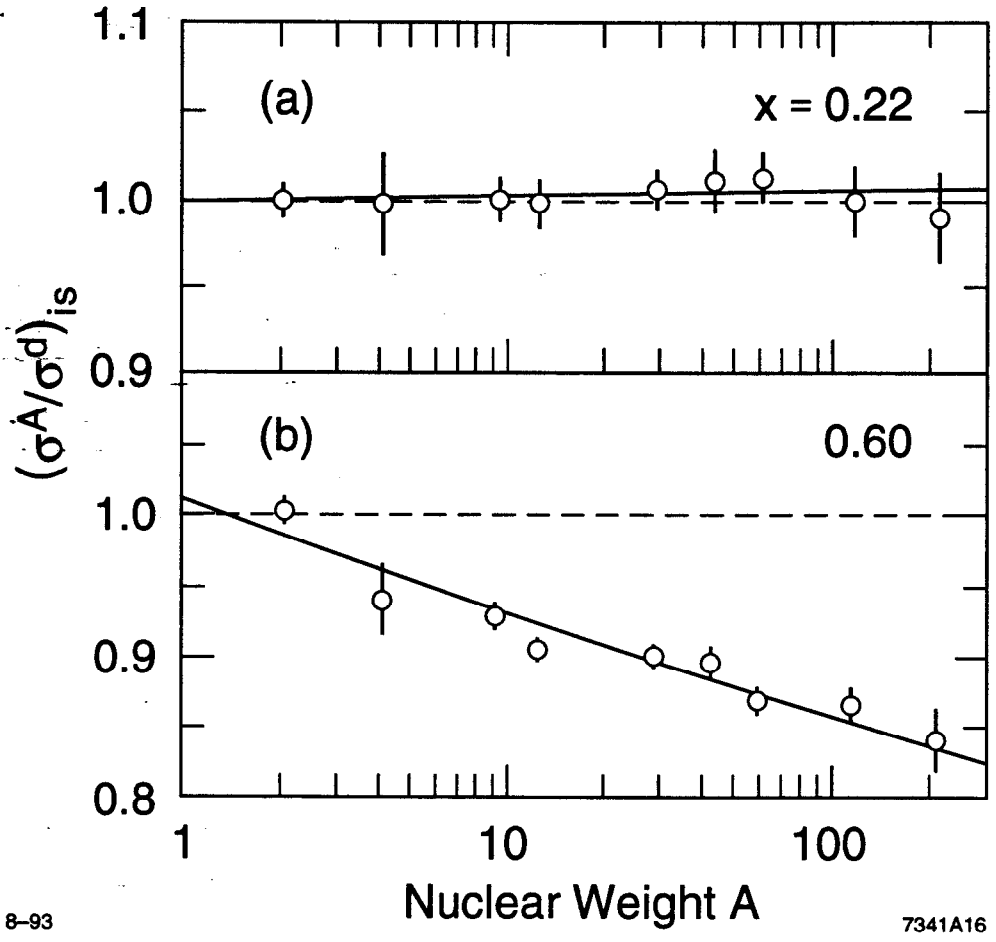
1.1
1.0
0.9
0.8
(a)
x = 0.22
(b)
0.60
$(\sigma^A/\sigma^d)_{is}$
1
10
100
Nuclear Weight A
8–93
7341A16

Fig. 18

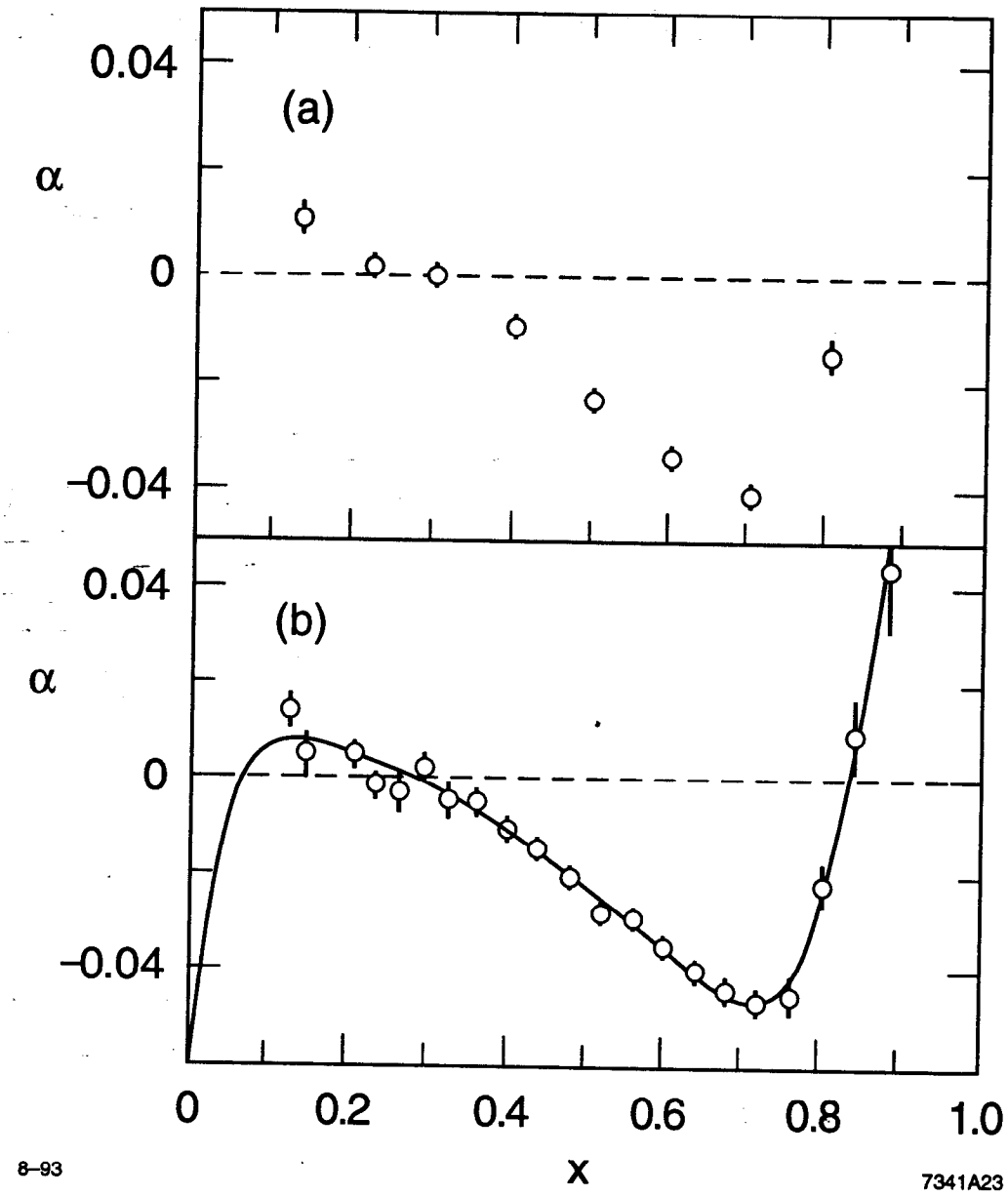

Fig. 19

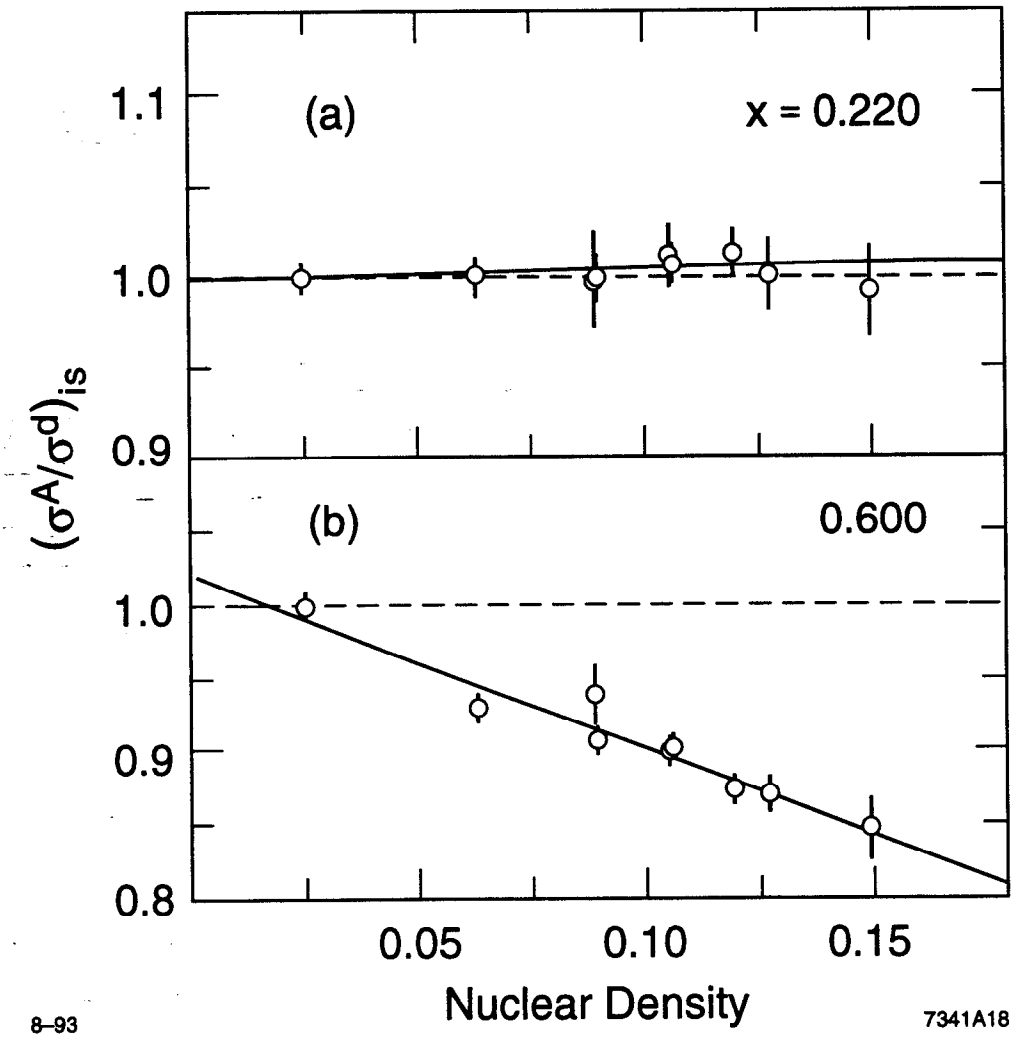
1.1
1.0
0.9
(a)
x = 0.220
$(\sigma^A/\sigma^d)_{is}$
(b)
0.600
1.0
0.9
0.8
0.05
0.10
0.15
Nuclear Density
8–93
7341A18

Fig. 20

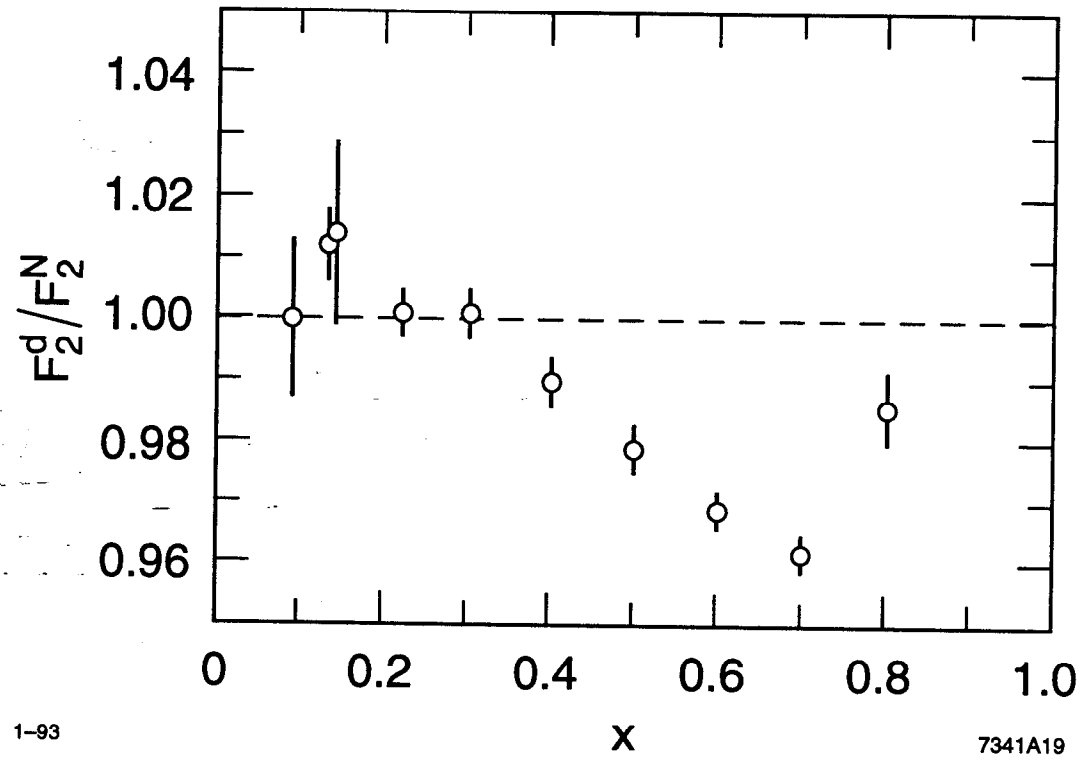

Fig. 21

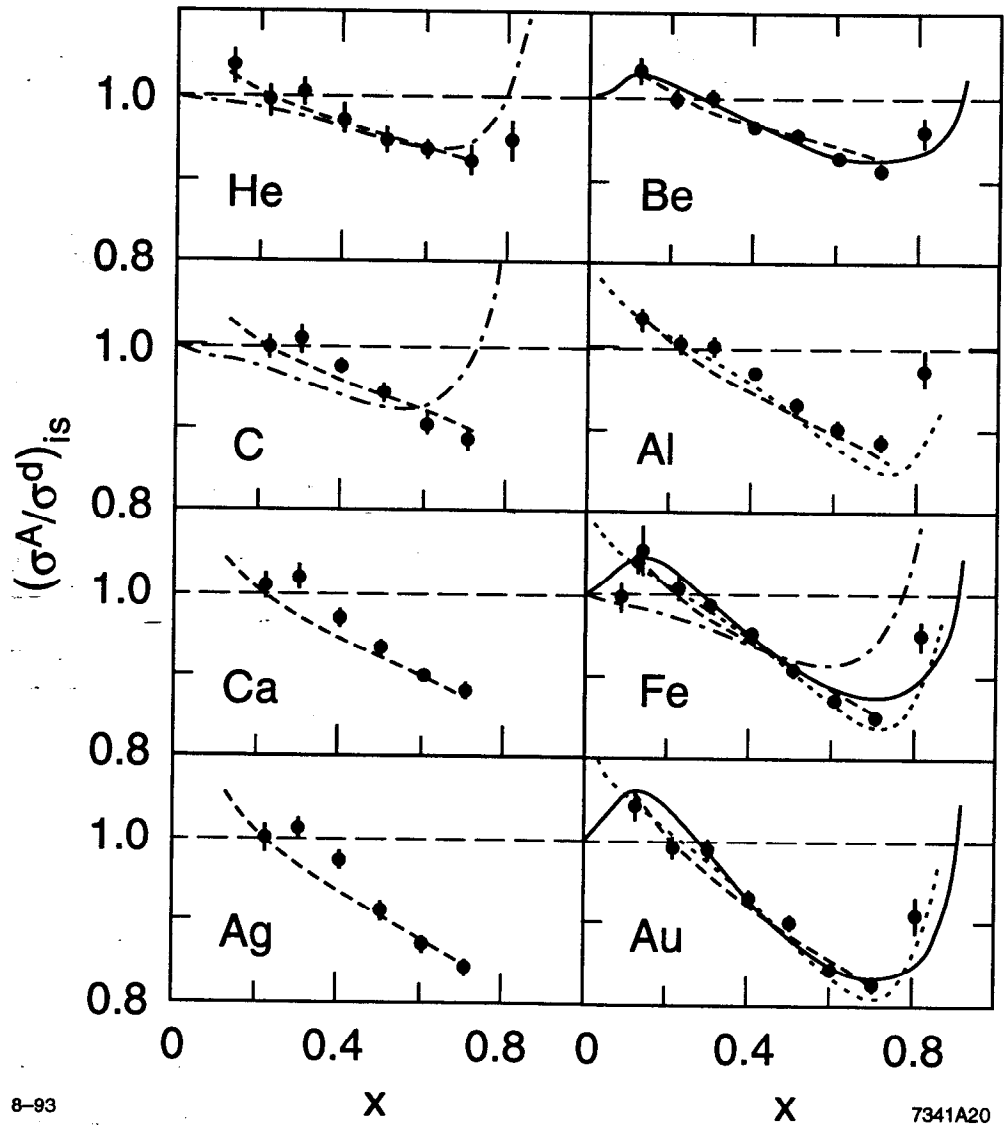

Fig. 22